

Kennesaw State University

DigitalCommons@Kennesaw State University

Master of Science in Chemical Sciences Theses

Department of Chemistry and Biochemistry

Spring 5-1-2019

Design of Cotton Fabric-Based Binary and Ternary Composite Materials Containing Nanostructured ZnO, TiO₂, and Plasmonic Nanoparticles: Photocatalytic Applications

Latanya Downer

Follow this and additional works at: https://digitalcommons.kennesaw.edu/mscs_etd



Part of the [Chemistry Commons](#), and the [Environmental Health Commons](#)

Recommended Citation

Downer, Latanya, "Design of Cotton Fabric-Based Binary and Ternary Composite Materials Containing Nanostructured ZnO, TiO₂, and Plasmonic Nanoparticles: Photocatalytic Applications" (2019). *Master of Science in Chemical Sciences Theses*. 23.

https://digitalcommons.kennesaw.edu/mscs_etd/23

This Thesis is brought to you for free and open access by the Department of Chemistry and Biochemistry at DigitalCommons@Kennesaw State University. It has been accepted for inclusion in Master of Science in Chemical Sciences Theses by an authorized administrator of DigitalCommons@Kennesaw State University. For more information, please contact digitalcommons@kennesaw.edu.

Design of Cotton Fabric-Based Binary and Ternary Composite Materials Containing
Nanostructured ZnO, TiO₂, and Plasmonic Nanoparticles:
Photocatalytic Applications

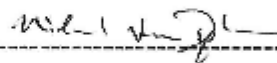
By

LaTanya Downer
Bachelors of Science in Chemistry
Savannah State University, 2016

Submitted in Partial Fulfillment of the Requirements
For the Degree of Master of Science in Chemical Science in the
Department of Chemistry and Biochemistry
Kennesaw State University
May 2019



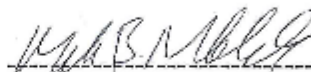
Committee Chair



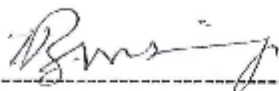
Graduate Program Coordinator



Committee Member



Department Chair



Committee Member



College Dean

Design of Cotton Fabric-Based Binary and Ternary Composite Materials Containing
Nanostructured ZnO, TiO₂, and Plasmonic Nanoparticles:
Photocatalytic Applications

By

LaTanya Downer
Bachelors of Science in Chemistry
Savannah State University, 2016

Submitted in Partial Fulfillment of the Requirements
For the Degree of Master of Science in Chemical Science in the
Department of Chemistry and Biochemistry
Kennesaw State University
May 2019

Committee Chair

Graduate Program Coordinator

Committee Member

Department Chair

Committee Member

College Dean

ACKNOWLEDGEMENT

Here, within this thesis lies the growth of Latanya Downer.

I would first like to acknowledge myself for all my hard work and dedication to achieving this accomplishment. It has not always been an easy journey. However, I did not quit. I just *turnt* the music up and kept driving towards my aspirations. I have always had a passion for chemistry, even though most times it felt like mastering a new mechanism. If you don't get it on the first try, don't quit because anything worth having is worth working towards. Because like Malcolm X once said, "education is the passport to the future, for tomorrow belongs to those who prepare for it today."

Dr. Bharat Baruah for all the support and help throughout this process.

Any members within the Baruah's lab that assisted towards the completion of my project.

Dr. Huggins Msimanga and Dr. Altug Poyraz for their assistance throughout my project.

The Poyraz group for helping with instrument related questions.

Mommy, Diane Diatta, and Oluwatobi Fabunmi for all the moral support.

Kennesaw State University's Department of Chemistry and Biochemistry for providing me with this opportunity

Funding

KSU CSM Mentor Protégé (BARUAH-01-FY2018-08) award
Research Stimulus Program (RSP) fund

"Turn every NO into a YES"

ABSTRACT

Nanostructure metals and metal oxides can be used for surface functionalization and combined with different materials to increase functionality. Recently, surface functionality has been of interest due to its multi-component and its ability to generate new material properties. One of its main application is the creation of nanomaterials because of its novel physical properties which contribute towards stabilization, strength, and catalytic properties. Nanomaterials makes it possible to fabricate objects in the nanoscale size range which offers beneficial physical properties. The nanomaterial distinctiveness allows for the creation of materials with unique characteristics for different applications such as photocatalytic coatings. Semiconductor and metal nanoparticles in heterogeneous systems have gained wide recognition in recent years because of their morphology-dependent electronic properties and their ability to integrate on various materials to improve functionality. Metal oxides, such as titanium (IV) oxide (TiO_2) and zinc oxide (ZnO) have received much attention due to their chemical stability, non-toxicity, low-cost, and high catalytic activity. In this report, we design binary and ternary composite materials on cotton fabric (CF) namely $\text{CF@TiO}_2\text{-AuNPs}$, and $\text{CF@ZnONRs-TiO}_2\text{-AuNPs}$. In these composite materials, the nanostructured TiO_2 and ZnO nanorods (ZnO-NRs) are deposited on CF by following *in-situ* method. Gold nanoparticles (AuNPs) are incorporated on the TiO_2 or ZnO-NRs by *in-situ* synthesis. The nanocomposite materials will be characterized by scanning electron microscopy (SEM), energy dispersive X-ray (EDX) line analysis, and X-ray diffraction (XRD). The photocatalytic degradation of aqueous Rhodamine B (RhB) will be assessed by UV-visible spectroscopy at room temperature under a UV lamp. It was found that the ternary system $\text{CF@ZnONRs-TiO}_2\text{-AuNPs}$ exhibit the best photocatalytic performance in comparison to the binary system $\text{CF@TiO}_2\text{-AuNPs}$.

Contents

ACKNOWLEDGEMENT	ii
ABSTRACT.....	iii
LIST OF TABLES/LIST OF FIGURES/ LIST OF SCHEME.....	vi
LIST OF KEY ACRONYMS	viii
CHAPTER 1. INTRODUCTION	3
1.1 Surface Functionalization.....	3
1.2 Photocatalytic Process.....	3
1.3 Titanium Dioxide	6
1.4 Zinc Oxide.....	8
1.5 Nanocomposite.....	10
1.6 Photocatalytic Activity of Semiconductor	11
1.7 Thesis Aim	13
CHAPER 2. INSTRUMENTATIONS	14
2.1 Principles of X-ray Diffraction.....	14
2.2 Principles of Scanning Electron Microscopy and Energy Dispersive X-ray Analysis 15	
2.3 Principles of UV-Visible Spectroscopy	16
CHAPTER 3. BINARY SYSTEM	19
3.1 Binary Composite.....	19
3.2 MATERIALS AND METHODS	21
A. Materials.....	21
B. Synthesis of TiO ₂ -nanosols	22
C. Pretreatment and Fabrication of CF@TiO ₂ Substrate.....	22
D. <i>In-situ</i> Deposition of Gold Nanoparticles	24
E. Characterization	25
F. Photocatalytic Study.....	26
3.3 RESULTS AND DISCUSSION	27
A. XRD Analysis	27
B. SEM Images	28
C. EDX Line Analysis	29
D. Photocatalytic Activity.....	30
3.4 CONCLUSION	33

CHAPTER 4. TERNARY SYSTEM.....	34
4.1 Ternary Composite	34
4.2 MATERIALS AND METHODS	36
A. Materials.....	36
B. Synthesis of ZnO Seeds Solution.....	37
C. Synthesis of ZnO Growth Solution	37
D. Synthesis of TiO ₂ -nanosols	37
E. Synthesis of Radical Scavengers.....	38
F. Pretreatment	38
G. Fabrication of CF@ZnONRs-TiO ₂ Substrate	38
H. <i>In-situ</i> Deposition of AuNPs.....	40
I. Characterization	41
J. Photocatalytic Study.....	41
K. Gold Ion Leaching Experiment.....	41
4.3 RESULTS AND DISCUSSION	41
A. XRD Analysis	42
B. SEM Images	44
C. EDX line Analysis.....	45
D. Photocatalytic Activity.....	48
E. Gold Leaching Expeirment	50
F. Radical Trapping of Ternary Nanocomposite.....	51
4.4 CONCLUSION.....	52
References.....	53
Appendix A.....	58
Appendix B	62

LIST OF TABLES/LIST OF FIGURES/ LIST OF SCHEME

Table 1.1. List of commonly used semiconductors	5
Table 3.1. EDX line analysis data for binary composite	30
Table 4.1 EDX line analysis data for binary composite	47
Figure 1.1. Band gap position of different semiconductors.....	5
Figure 1.2. The schematic conventional cells for TiO ₂	7
Figure 1.3. The schematic conventional cells for ZnO	9
Figure 1.4. Illustration of a core/shell	11
Figure 1.5. Illustration of a photocatalytic reaction mechanisms	12
Figure 2.1. Schematics of an angled X-ray diffractometer	15
Figure 2.2. Diagram of possible electronic transitions	18
Figure 2.3. Schematic of UV-Visible spectrophotometer.....	18
Figure 3.1. Process for the fabrication of CF@TiO ₂	23
Figure 3.2. Digital photography of CF@TiO ₂	23
Figure 3.3. Digital photography of CF@TiO ₂ -AuNPs	25
Figure 3.4. Molecular structure of RhB	26
Figure 3.5. XRD pattern of binary system	28
Figure 3.6. SEM images of binary system	29
Figure 3.7. UV-Visible adsorption spectra binary system	32
Figure 4.1. Process for the fabrication of CF@TiO ₂	39
Figure 4.2. Digital photography of CF@TiO ₂	39
Figure 4.3. Digital photography of CF@TiO ₂ -AuNPs	40
Figure 4.4. XRD pattern of binary system	43

Figure 4.5. SEM images of ternary system	45
Figure 4.6. UV-Visible adsorption spectra binary system	49
Figure 4.7. UV-Vis adsorption spectrum for gold ion	50
Figure 4.8. Radical trapping of CF@ZnONRs-TiO ₂ -AuNPs	51
Scheme 2.1. Illustration of EDX X-ray generation	16
Scheme 3.1. Graphic of TiO ₂ and AuNPs	21
Scheme 3.2 Illustration of AuNPs.....	24
Scheme 4.1. Illustration of ZnONRs-TiO ₂ -AuNPs.....	36
Scheme 4.2 Illustration of AuNPs	40

LIST OF KEY ACRONYMS

UV: Ultra-violet	e^-_{CB} : Electron of conductance band
$OH\cdot$: Hydroxyl radical	h^+_{VB} : Hole of valence band
O_2 ; Oxygen gas	CF: Cotton fabric
$O_2^{\cdot-}$: Superoxide anion	AuNPs; Gold nanoparticles
Si: Silicon	NPs: Nanoparticles
TiO_2 : Titanium Dioxide or titania	LSRP: Localize Surface Plasmon Resonance
ZnO: Zinc oxide	RhB: Rhodamine B
WO_3 : Tungsten trioxide	XRD: X-ray diffraction
Cds: Cadmium sulfide	SEM: Scanning electron microscopy
ZnS: Zinc sulfide	EDX: Energy dispersive X-ray
VLA: Visible light active	UV-Vis: Ultraviolet-visible
Zn: Zinc	$NaAuCl_4 \cdot 2H_2O$: Sodium tetrachloroaurate
O: Oxygen	dihydrate
C: Carbon	

CHAPTER 1. INTRODUCTION

1.1 Surface Functionalization

Surface functionalization of nanostructured metals and metal oxides can be combined with different materials within the same structure, as a way to increase functionality. There has been much interest in surface functionality because of its multi-component and its ability to generate new material properties. These novel physical properties play a significant role in stabilization, strength, catalytic, and high specific chemical reactivity in other materials including biospecies and nanomaterials.¹ For the applications of biosensor fabrication, surface functionalization of nanostructured materials can present numerous functional or organic groups and can enhance hydrophilicity to anchor biomolecules through forming specific bonds or electrostatic interactions or by grafting or ligands on nanostructured materials.¹

Nanomaterials make it possible to employ materials on an atomic or molecular scale to generate objects in the nanoscale size mode (1-100 nm); these materials show interesting quantum effects.² The nanoscale size offers beneficial physical properties for it has an enormous surface area, which is extremely reactive in comparison to other more massive forms. The small magnitude of the nanomaterials contributes to the formation of familiar mixtures with various materials to magnify the properties of the material. The nanomaterial uniqueness allows for the creation of materials with distinctive characteristics for multiple applications such as barrier coating, self-cleaning hydrophobic or photocatalytic coatings, antistatic coatings, and superparamagnetic coating.³

1.2 Photocatalytic Process

The photocatalytic degradation process has gained much interest in the field of wastewater treatment, particularly for wastewater containing toxic aromatic compounds and organic

substances. This process involves the acceleration of a photoreaction in the presence of a catalyst, which allows for the degradation of obstinate organic pollutants into carbon dioxide and water, by utilizing visible and/or ultra-violet (UV) light.^{4,5} The photocatalytic process offers several advantages such as no waste disposal, low cost, complete mineralization, low temperature and pressure conditions.^{4,5}

Photocatalyst focuses on the use of metal oxide semiconductor for the degradation of refractory organic substances. For a semiconductor to be photochemically active as a sensitizer in a photoreaction the redox potential of the photogenerated valence band hole must be sufficiently positive to generate hydroxyl (OH^\cdot) radicals; which can subsequently oxidize the organic pollutants.⁴ While the redox potential of the photogenerated conduction band electron must be adequately negative to be able to reduce absorbed oxygen gas (O_2) to superoxide ($O_2^{\cdot-}$).⁴ Photocatalytic semiconductors such as Si, TiO_2 , ZnO , WO_3 , CdS , and ZnS have attracted vast scientific significance due to their photocatalytic functions.⁴ Table 1 lists the band gap energies, wavelength, valence and conduction band and figure 1 lists the band gap positions of said catalysts and provides the redox potentials of the H_2O/OH^\cdot and O_2/HO_2^- couples.

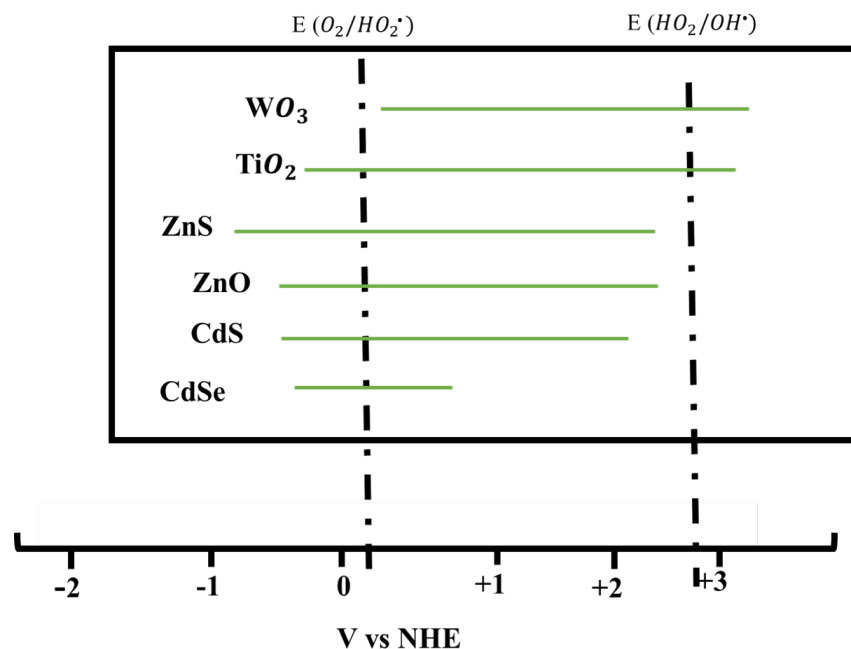


Figure 1.1. Band gap position of different semiconductors and O_2/HO_2^\bullet and H_2O/OH^\bullet couple. Adopted from Bhatkhande *et al.*⁴

Table 1.1 List of commonly used semiconductors in the photocatalysis process. Adopted from Daghrir *et al.*⁶

Photocatalyst	Band gap (eV)	Wavelength (nm)	Valence band (V vs NHE)	Conduction band (V vs NHE)
TiO ₂	3.2	387	+3.1	-0.1
ZnO	3.3	387	+3.0	-0.2
Cds	2.5	496	+2.1	-0.4
SnO ₂	3.8	318	+4.1	+0.3
ZnS	3.7	335	+1.4	-2.3
WO ₃	2.8	443	+3.0	+0.4
CdSe	2.5	729	+1.6	-0.1

1.3 Titanium Dioxide

Titanium Dioxide, also known as titanium (IV) oxide or titania, is a renowned and well-studied semiconductor due to its chemical stability, non-toxicity, low cost, biocompatibility, physical, optical, and electrical properties.⁷ Titania has a strong oxidation and reduction capabilities for photoexcitation. Fujishima and Honda first observed this phenomenon in 1972 when they validated the potential of TiO₂ semiconductor material to split water into hydrogen and oxygen in a photoelectrochemical cell.⁸ Since then their research has sparked an interest in advance of semiconductor photocatalysis for a wide array of energy and eco-friendly applications.⁷ With the development of visible light active (VLA) TiO₂ photocatalytic material being the most scientific and monetary advances.⁸ The systematic photocatalytic process of titania has various advantages and applications. However, one of its main area of focus is the decomposition of unwanted and refractory organic substances, destruction of pollutants from wastewater and air, the killing of harmful bacteria and cancer cells.⁷

TiO₂ is known to be an *n*-type semiconductor due to oxygen deficiency which is compensated by the presence of Ti³⁺ centers.⁸ It exists in three polymorphs: anatase, rutile, and brookite (fig. 1.2). All three mineral forms can be synthesized in a laboratory setting; anatase type is constructed of the corner (vertices) sharing octahedral which form (001) planes resulting in a tetragonal structure (with dipyramidal habit)^{7,8} and is used primarily as a photocatalyst under UV irradiation.⁷ In rutile, the octahedral share edges at (001) planes to give a tetragonal crystal structure (with prismatic habit).^{7,8} This form is primarily employed as a white pigment in paint.^{7,8} In brookite both edges and corners are shared to give an orthorhombic crystalline structure.⁸ The band gap for anatase is 3.2 eV, 3.0 eV for rutile, and ~3.2 eV for brookite.⁸ Anatase polymorphs is the preferred form due to its high photocatalytic activity because it has a more negative

conduction band edge potential and high specific area.⁷ Titania, thus, has a variety of usage in different products such as solar cell, food coloring agent, electrochemical electrodes, and capacitors.⁷

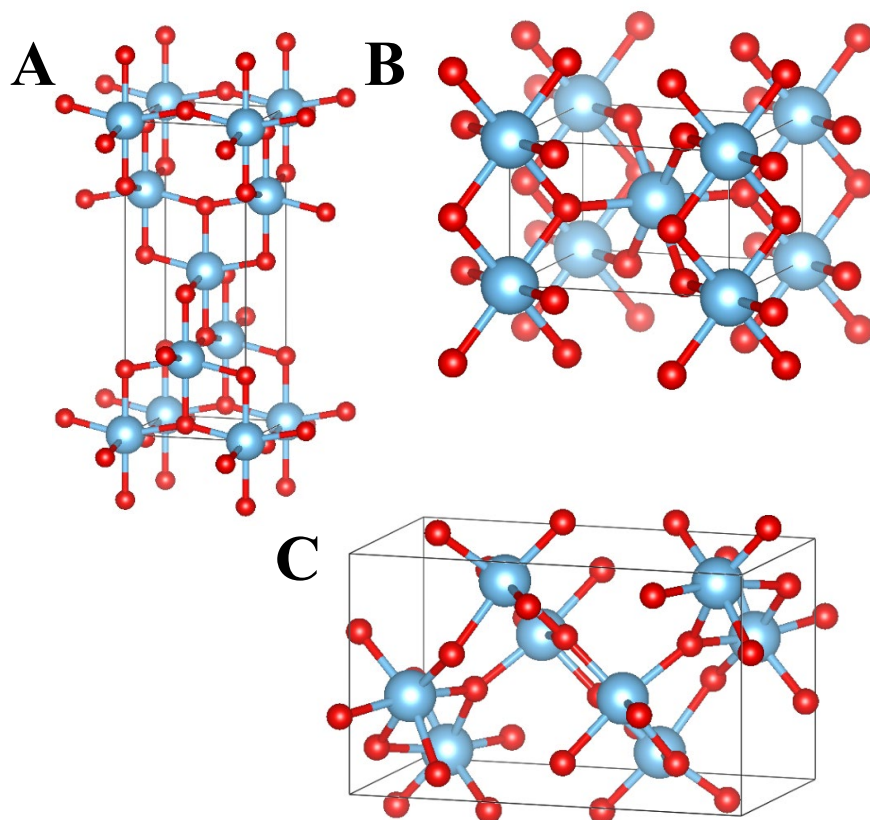


Figure 1.2. The schematic conventional cells for: (a) anatase, (b) rutile, (c) brookite. The larger blue spheres represents Ti atoms and the smaller red spheres represents O atoms.

The intrinsic properties of TiO_2 lead to limitations that restrict its applications.⁹ Titania has two major limitations, first, the absence of visible-light response, due to its wide band gap (3.2 eV for anatase). Wide band gap restricts the photocatalytic activity to the UV-light region and diminishes the option to feat full solar radiation to impel photocatalysis.⁹ Second, the fast

recombination rate of photogenerated electron-hole pairs which decrease the overall quantum yield of TiO₂.⁹

1.4 Zinc Oxide

Numerous heterogeneous photocatalysis has been investigated due to their ability to degrade refractory organic substance in an aqueous medium with high proficiency. TiO₂ is the most common photocatalyst; however, a recent examination has revealed that zinc oxide (ZnO) could be a better substitute semiconductor for prospective photocatalyst because of its distinctive physical and chemical properties.^{5,10} Such features include high electrochemical coupling coefficient, high catalytic activity, UV filtering properties, and high photostability.¹¹ In comparison to TiO₂, ZnO has been increasingly compelling because it absorbs exceedingly over the UV spectrum and absorbs more light quanta than TiO₂.¹² Though more effective ZnO has photocorrosion at pH lower than 4.¹² The materialization of zinc ion is ascribed to the oxidation of zinc oxide by the valence band.¹²

Zinc oxide is an *n*-type semiconductor that is classified as an II-VI semiconductor whose covalence shows firm ionic bonding and light covalent character.¹³ Its semiconductor group characteristic is attributed to zinc (Zn) and oxygen (O) being in separate groups on the periodic table.¹³ ZnO offers excellent piezoelectric, electric conductivity, chemical sensing, optical, and semiconductor properties.¹³ ZnO has a wide band gap of 3.3 eV in the near-UV spectrum, bulky exciton binding energy of 60 meV, an electron affinity of 4.2 eV, and high thermal and mechanical stability at ambient temperature making it a favorable material for a variety of applications in diverse fields.^{11,13} The electrical conductivity and optical absorption of ZnO is affected due to its wide band gap, when the catalyst is doped with other metals there is an increase in its conductivity and the excitonic emission can increase at room temperature.¹³ ZnO holds

higher optical absorption in the UVA (315-400 nm) and UVB (280-315 nm) regions which are favorable in photoreactions.¹³

Nano-ZnO has been synthesized in various growth morphologies such as nanoneedles, nanosphere, nanotubes, nanowires, and nanorods each with specific structural, optical, electrical, and physicochemical properties.¹³ Zinc oxide exists in three polymorphs: wurtzite (fig. 1.3A), zinc-blende (fig. 1.3B), and sometimes rock-salt. Wurtzite ZnO, most stable, has a hexagonal structure with lattices spacing $a = 0.325$ nm and $c = 0.521$ nm, the fraction $c/a \sim 1.6$ is considered close to the model value for hexagonal cell $c/a = 1.633$.^{13,14} The structure is presented as an integer of interchanging planes made of tetrahedrally coordinated oxygen and zinc ions, arranged to interchange along the c -axis.^{13,14} The tetrahedral organization creates a non-central symmetric structure and thus piezoelectricity and pyroelectricity.^{13,14} Wurtzite ZnO as a polar surface with a basal plane. Zinc-blende ZnO has a face-centered cubic structure and has no inversion symmetry.^{13,14}

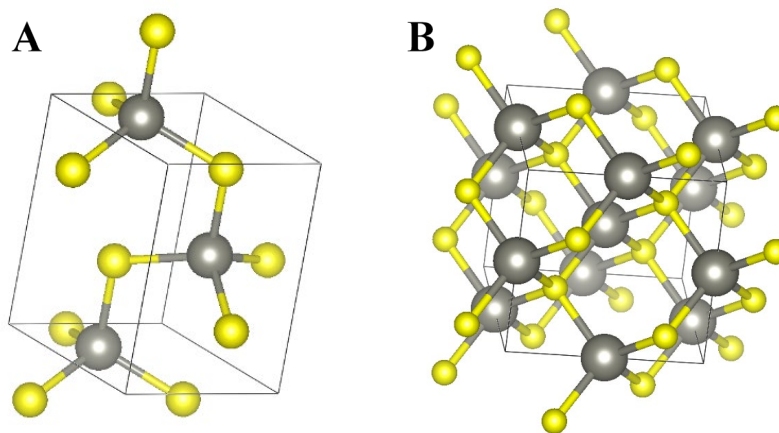


Figure 1.3. The schematic conventional cells for: (a) Wurtzite, (b) zinc-blende. The larger gray spheres represents Zn atoms and the smaller yellow spheres represents O atoms.

1.5 Nanocomposite

Semiconductor and metal nanoparticles in heterogeneous systems have gained full recognition in recent years because of their morphology dependent electronic properties and their ability to integrate on various materials to improve functionality.^{15,16} This fabricated system is of an advantage because it appreciably enhances the capping of the semiconductor or metal nanocluster with another layer of compatible material, which leads to better stability of the nanoparticles.¹⁵ With this advantage, composite nanoclusters provide several applications such as xerography, photography, chemical synthesis, and conversion and storage of solar light energy.¹⁶ There has been much development in this field, which has led to the design of different core/shell type nanomaterials, for instance, metal/metal, metal/semiconductor, metal/metal oxide, semiconductor/semiconductor, and semiconductor/metal systems.¹⁵

The main aim of designing and improving the composite material is their capability to enhance the catalytic properties or to adjust the luminescent or sensing properties.¹⁵ Kamat *et al.* cited that single integral semiconductor demonstrates moderately poor photocatalytic efficiency (<5%) for most of the photogenerated charge carriers undergo recombination.¹⁶ For example, reactive surfaces, such as titania are capable of undergoing charge-transfer interaction with specific functional groups of the adsorbed molecule because of their hydroxylated surfaces.¹⁶ This phenomenon can be a probe with electronic absorption and emission as the energetics of the ground and excited states are modified.¹⁶ However, a semiconductor/metal composite material aids charge correction in the system.¹⁵ If a semiconductor is decorated with noble metal (e.g., gold or silver) it will increase the efficiency of the photocatalytic reactions.¹⁵ The noble metal has a high electron storage capacity within its particle; therefore, it functions as a sink for photoinduced charge carriers, supporting interfacial charge-transfer process.¹⁵ Composite materials have been proven

to improve the photoconversion efficiency of dye-sensitized photoreaction and photochemical solar cells.¹⁵

Dawson *et al.* reported that though much effort has been made to fabricate semiconductor/metal composite nanoparticles, there is still limited knowledge available about the photodynamic of the materials.¹⁵

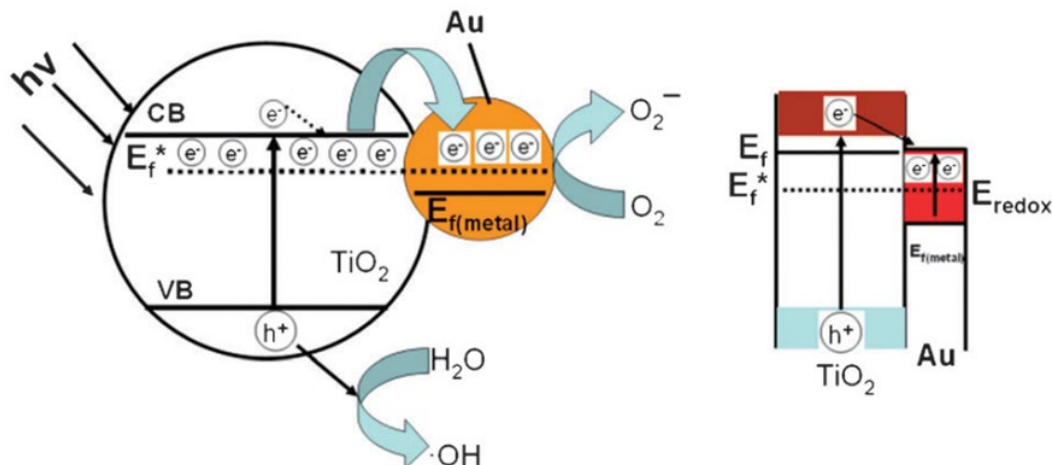


Figure 1.4. Illustration of a core/shell semiconductor/metal nanomaterial. Adopted from Abdulla-Al-Mamun *et al.*¹⁶

1.6 Photocatalytic Activity of Semiconductor

The photocatalytic activity of a semiconductor is induced by light excitation. The light energy must be equal or higher than the band gap energy of the semiconductor, which leads to the formation of electron-hole pair.^{3,8} Since titania is only active in the UV region, UV light ($\lambda \leq 387$ nm) is necessary.⁸ While ZnO holds higher optical absorption in the UVA (315-400 nm) and UVB (280-315 nm) regions.¹³ The photoinduced reaction is activated by the absorption of a photon that excites an electron to the conduction band (e^-_{CB}) forming a positive hole in the valence band (h^+_{vB}) of the semiconductor catalyst.^{7,8} For titania the absorption leads to charge separation where the charge carriers can be confined as Ti^{3+} and O^- defected site with the titania lattices or

recombined.⁸ A redox reaction with the adsorbates can occur if the charge carriers transfer to the catalyst surface.^{7,8}

The catalyst can interact with light of sufficient energy to produce reactive oxidizing species that can lead to the photocatalytic transformation of a pollutant.^{7,8} During the photoinduced reaction two processes can transpire concurrently, first involves the oxidation of dissociatively absorbed water by photogenerated holes and second involves the reduction of an electron acceptor by photoexcited electrons. These reactions lead to the production of a $\cdot\text{OH}$ and $\text{O}_2^{\cdot-}$ radical anion.⁸ The $\cdot\text{OH}$ is vastly robust oxidants.⁸ They can successively oxidize organic species with mineralization producing minerals salts, CO_2 , and H_2O .⁸ While the $\text{O}_2^{\cdot-}$ can contribute to the oxidative pathway, for instance the degradation of a pollutant.⁸

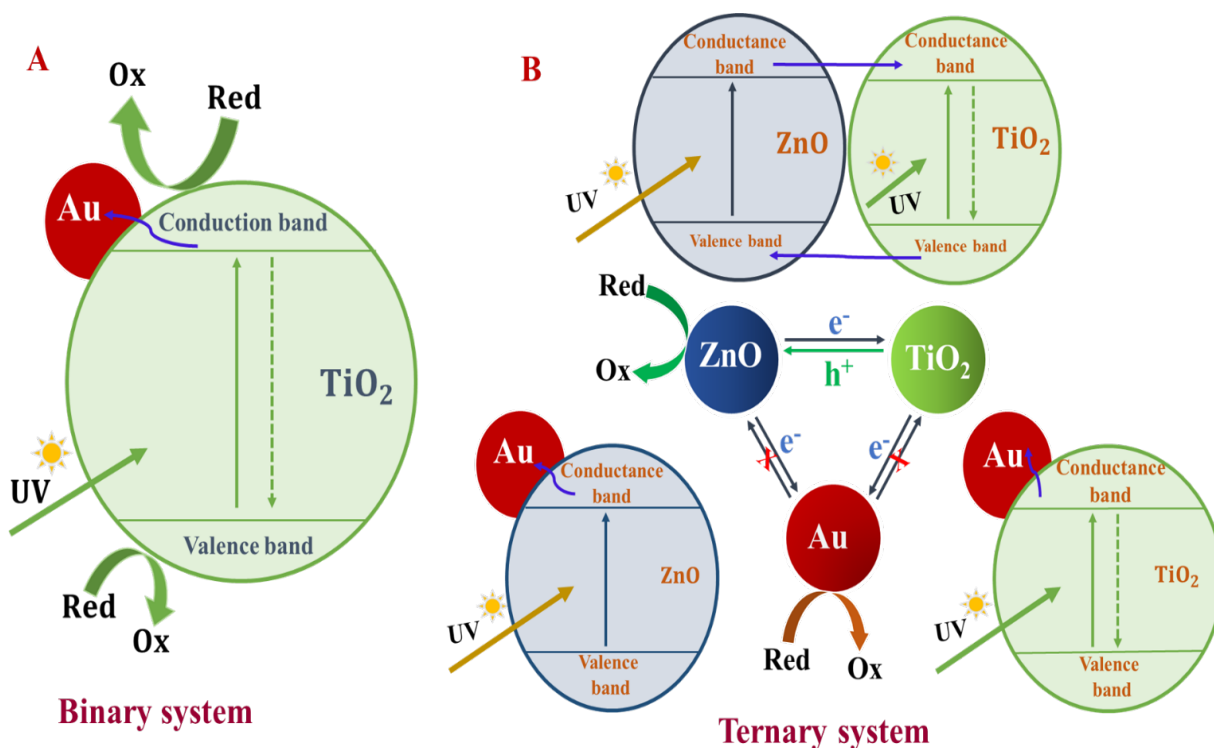


Figure 1.5. Illustration of a photocatalytic reaction mechanisms for: A) binary system and B) ternary system.

1.7 Thesis Aim

The objective of this thesis work is to design a semiconductor/metal nanoparticle system capable of enhancing catalytic and sensing properties and assessing their ability to degrade Rhodamine B (RhB) as an organic pollutant in water. TiO₂ and ZnO will be used as a semiconductor component. However, since single integral semiconductor exhibits weak photocatalytic efficiency gold nanoparticles (AuNPs) will be incorporated into the system to increase the efficiency of the photoreaction.¹⁶ We create binary and ternary composite material on functionalized cotton fabric (CF) namely CF@TiO₂-AuNPs, and CF@ZnONRs-TiO₂-AuNPs. The use of a functionalized textile makes a more innovative system because it eliminates the need to centrifuge, filter, and better recovery after degradation. Besides, the CF-based composites are excellent for recyclability. CF@TiO₂-AuNPs and CF@ZnONRs-TiO₂-AuNPs are expected to have no charge-transfer interaction and enhanced photocatalytic activity over CF@TiO₂ and CF@ZnONRs-TiO₂ due to the addition of the noble metal. This thesis will be structured as follows: Chapter one will discuss the literature review on heterogeneous photocatalysis, nanocomposite and their photocatalytic activity. Chapter two will detail the principles of characterization techniques. Chapter three will detail the binary system. Chapter four will describe the ternary system, gold ion leaching, and radical trapping^{17,18} experiment of the most active composite.

CHAPTER 2. INSTRUMENTATIONS

2.1 Principles of X-ray Diffraction

In 1912, Max von Laue and colleague discovered X-ray diffraction (XRD) by crystals, they proved that crystalline substances act as a three-dimensional diffraction grating for X-ray wavelengths of equivalent magnitude to the spacing of planes in a crystal lattices.¹⁹⁻²¹ Following this discovery, William Henry Bragg and his son William Lawrence Bragg developed an alternative technique, Bragg's law, to which contributed to the confirmation of Laue findings.¹⁹⁻²¹

X-ray diffraction is a non-destructive analytical method used to establish evidence on the internal lattice of crystalline substances such as unit cell dimensions, bond-lengths, bond-angles, and crystal defects.¹⁹⁻²¹ The technique uses X-ray analysis to generate a crystal structure by using the diffraction data provided from the interaction between a crystalline structure and a beam of incident rays.¹⁹⁻²¹ Upon diffraction light is scattered by a periodic array with long-range order, generating constructive interference at specific directions.¹⁹⁻²¹ However, for this to occur Bragg's Law must be satisfied: $2d\sin\theta = n\lambda$, where d is the inter-planar spacing associated with the diffraction, θ is the diffraction angle, n is a positive integer, and λ is the wavelength of the incident wave.¹⁹⁻²¹ Based on the specific directions a reflection occurs which is due to the presence of spots on the diffraction pattern.¹⁹⁻²¹

As a result, X-ray diffraction occurs from the electromagnetic radiation affecting the regular array of scatters.¹⁹⁻²¹ Electromagnetic waves are utilized to create the diffraction pattern for their wavelength is considered the same order of magnitude as their lattice spacing between planes in a crystalline sample, Bragg's law is used to relate this concept.¹⁹⁻²¹ Because of this concept diffracted X-rays can be detected, processed, and counted.¹⁹⁻²¹ All probable diffraction direction of the crystal lattice can be obtained by scanning the sample through a range of 2θ angles

due to the random orientation of the sample material.¹⁹⁻²¹ The d-spacing generated is compared to a set of standard reference patterns.¹⁹⁻²¹ A compound can be identified based on the conversion of the diffraction peaks to d-spacing because each compound has a distinctive set of d-spacing.¹⁹⁻²¹

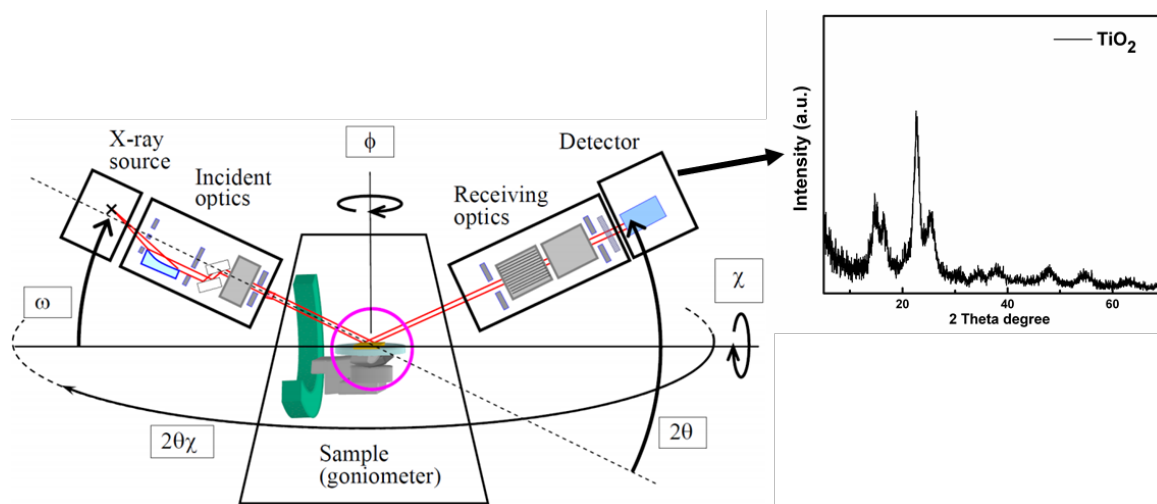


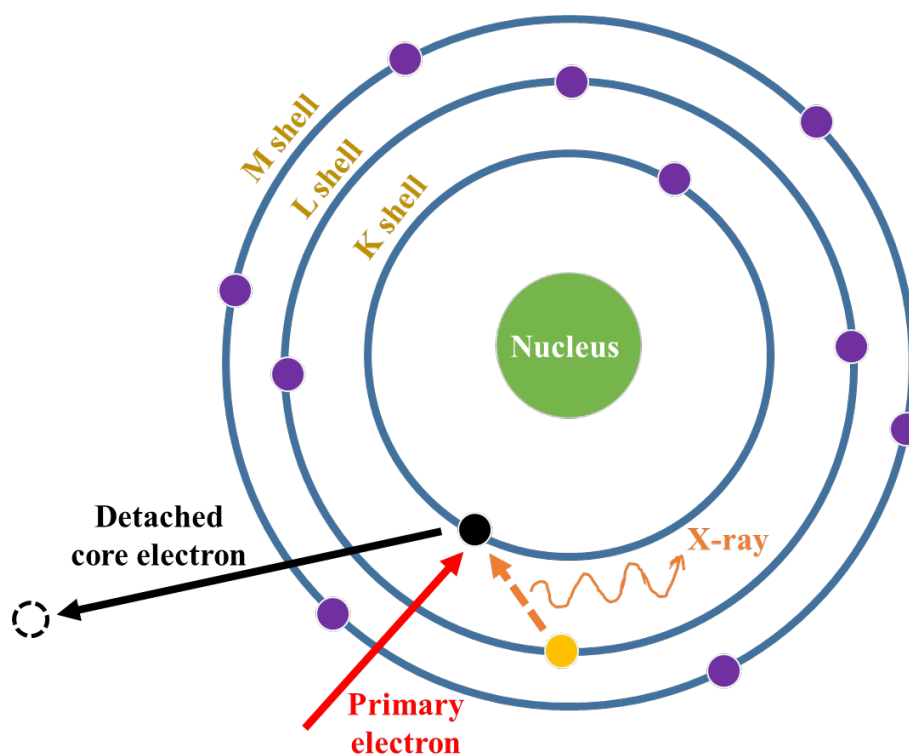
Figure 2.1. Schematics of an angled ($2\theta_x$ axis) X-ray diffractometer pattern using Bragg's law. Adopted from Inaba *et al.*²²

2.2 Principles of Scanning Electron Microscopy and Energy Dispersive X-ray Analysis

Scanning electron microscopy (SEM) is a rapid and non-destructive analytical technique used for nanoscale surface analysis.²⁰⁻²² The technique delivers high-resolution images of a specimen surface topography by scanning the surface with a highly focused beam of electron.²³⁻
²⁵ Those electrons will interact with the molecules in the specimen, fabricating numerous signals that produce data about the composition and surface topography of the specimen.²³⁻²⁵ The electron beam scans the sample in a parallel rectangular form, then use the beam locus and detected signals to generate a high-resolution image.²³⁻²⁵ The SEM can also be paired with an energy dispersive X-ray (EDX) spectroscopy system, this portion of the system is used for the determination of elemental identification and composition of a sample at the nanoscale, and map their dissemination.²³⁻²⁵ The technique is based on characteristic radiation, which occurs when outer-shell electrons are discharged to fill the opening in the inner shell of an atom, freeing radiations

in a pattern that is unique to each element.²³⁻²⁵ This form of X-ray is emitted during the analysis when the electron beam detaches an inner shell electron from the specimen.²³⁻²⁵ An electron with a higher-energy from the outer shell then packs the electron-hole in the inner shell with electrons.²³⁻²⁵ The instrument then measures the number of quanta and energy of the radiation. EDX is then able to measure the elemental composition using the energies of the X-rays because of its uniqueness to each emitting element.²³⁻²⁵

2.3 Principles of UV-Visible Spectroscopy



Scheme 2.1. Illustration of EDX X-ray generation process for analysis.

Ultraviolet-visible spectroscopy (UV-vis) is a well-known analytical technique used for chemical identification and qualitative analysis, one of its main applications is the quantitative determination of various organic and inorganic substances in an aqueous medium.²⁶⁻²⁹ The technique operates in the ultraviolet-visible gamut, meaning it uses light in the visible and

adjoining scope.²⁶⁻²⁹ UV-vis correlates the interaction of light with matter, leading to absorption or reflectance in the visible region of the electromagnetic spectrum where atoms and molecules undergo electronic transitions.²⁶⁻²⁹ This may transpire for the absorbed ultraviolet radiation energy is equal to the energy difference for the electronic transition states.²⁶⁻²⁹ When there is an absorption of light in the ultraviolet or visible region by a chemical substance a unique spectrum will be generated.²⁶⁻²⁹

Molecules can absorb the energy in the form of ultraviolet or visible light with bonding and non-bonding electrons excite the electrons to a higher anti-bonding molecular orbital.²⁶⁻²⁹ However, if a molecule contains a readily excited electron it can absorb a longer wavelength of light.²⁶⁻²⁹ There are four types of transition; $\pi - \pi^*$, $n - \pi^*$, $\sigma - \sigma^*$, and $n - \sigma^*$.²⁶⁻²⁹ The UV spectrophotometer uses Beers-Lambert law: $A = \log\left(\frac{I_0}{I}\right) = \epsilon lc$, where is the A for the absorbance of a sample at a specific wavelength: I_0 and I is the intensity of the monochromic light entering the sample and the intensity of the light emerging from the sample.²⁶⁻²⁹ The sample absorbance is directly related to the concentration of the absorbing substance and the pathlength of the sample according to the law: ϵ is the molar extinction coefficient ($M^{-1}cm^{-1}$), c is the concentration (M) of the solute, and l is the pathlength (cm).²⁶⁻²⁹

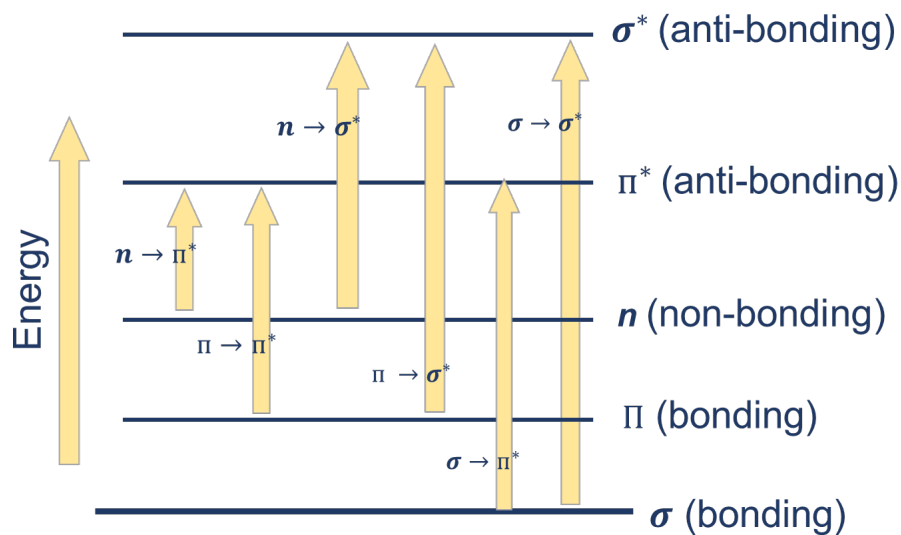


Figure 2.2. Diagram of possible electronic transitions of π , n , and σ electrons.

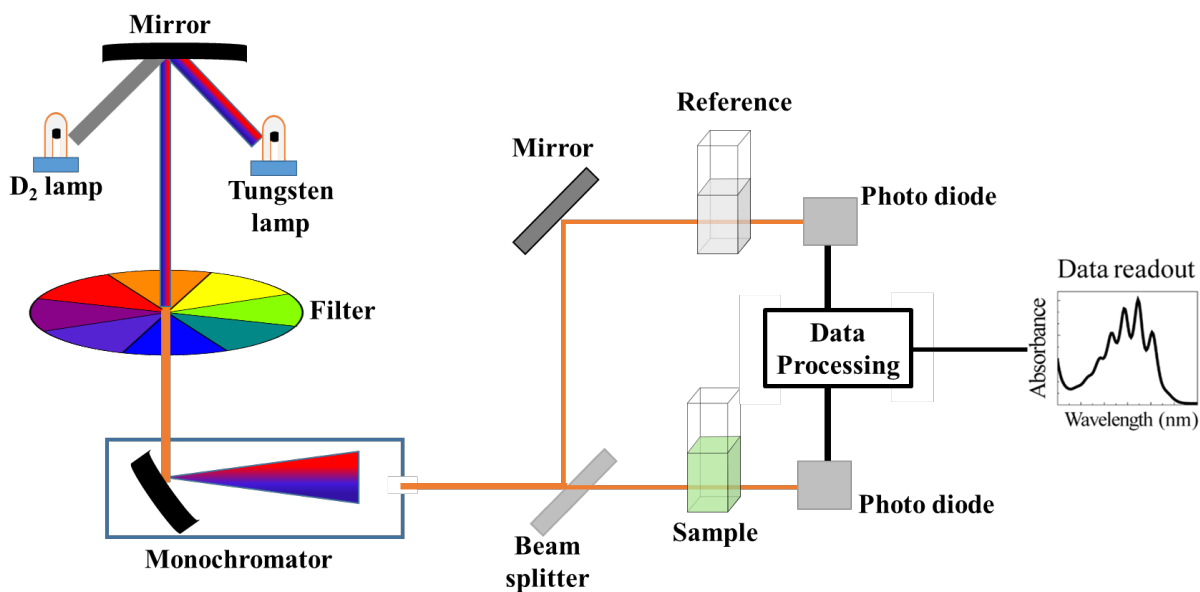


Figure 2.3. Schematic of UV-Visible spectrophotometer.³⁰

CHAPTER 3. BINARY SYSTEM

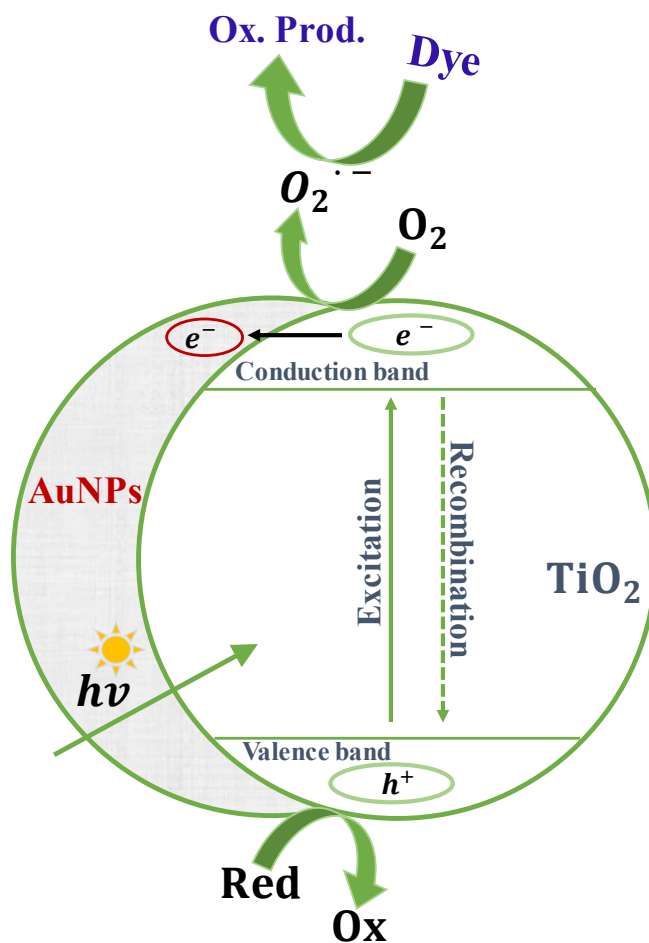
3.1 Binary Composite

The overuse of organic dyes for domestic purpose and industrial activities has led to severe environmental concerns. The over usage has led to water contamination because most dyes and their metabolites are toxic and carcinogenic and thereby endanger public health as well as imposing harmful consequences upon the ecosystem.³¹ In the past decade, the scientific community has made great efforts to develop energy efficient photocatalysts to treat industrial wastewater containing toxic aromatic compounds and organic dyes.³¹ Photocatalysis focuses on the use of metal oxide semiconductors for degradation of organic pollutants.³¹ Semiconductors photocatalysis such as TiO₂ has attracted much interest due to its high stability, low cost, and non-toxicity. The semiconductor would be employed in a photocatalytic degradation process as a way to degrade organic pollutants under near UV irradiation. However, there are several limitations to this process. First, titania has a wide band gap making it only active under UV irradiation thereby restricting its catalytic efficiency under visible light.³² Second, it undergoes electron-hole recombination in the absence of acceptable electron and hole scavengers leading to significant loss of stored energy which results in limited quantum yield for photoreactions.³² To rectify these limitations binary systems have been created using different core/shell type nanomaterials, for example, metal/metal and semiconductor/metal. A binary system using metal oxides supported noble-metal nanoparticles has been used to regulate the electronic band gap structure of titania thereby broadening the photosensitive response to the visible light region.^{32,33}

Lu *et al.* reported that gold (Au) and silver (Ag) noble-metal nanoparticles (NPs) can lead to visible light activation because of their localized surface plasmon resonance (LSPR). LSPR is caused by the oscillations of the surface electrons existing on the localized surface of the noble-metals NPs.³⁴ This phenomenon causes the red light to be intensely absorbed and dispersed,

making Au or Ag act as an antenna to harvest light leading to the extension of the light absorption gamut of the semiconductor wide band gap.³⁵ Julkapli *et al.* reported that TiO₂ supported AuNPs has given promising results because the AuNPs have high electron storage capacity and functions as a sink for the photoinduced charge carriers while promoting interfacial charge transfer process.³⁵ There is a decrease in the energy band gap of TiO₂ in the presence of AuNPs in comparison to the typical band gap energies of anatase and rutile TiO₂ (3.2 eV and 3.0 eV), this promotes robust interaction between AuNPs and TiO₂ while increasing the charge separation between the excited e^-_{CB} and h^+_{VB} enhancing the photocatalytic activity of the metal oxide.³³ The different Fermi levels of the semiconductor and noble metal NPS can be credited for the enhanced photocatalytic activity.³³ The Fermi level energy of the conduction band edge of titania is higher than AuNPs. Therefore, the photo-stimulated electrons can be trapped by AuNPs whereas the photo-formed holes stay in TiO₂ valence band.³³

For this project, we fabricate CF@TiO₂ and CF@TiO₂-AuNPs nanocomposite for the degradation of RhB, to evaluate the efficiency of the nanocomposite when it is decorated with AuNPs. We hypothesized that CF@TiO₂-AuNPs nanocomposite is a better system for the degradation of dye pollutants for there should be no electron-hole recombination and enhanced photocatalytic activity in comparison to CF@TiO₂ due to the addition of the noble-metal NPs.



Scheme 3.1. Graphic of TiO₂ and AuNPs interfacial charge transfer process.

3.2 MATERIALS AND METHODS

A. Materials

100% Cotton fabric used as a substrate, was purchased from a local Walmart. Sodium hydroxide beads, methanol, and Triton X-100 (Polyethylene glycol tert-octylphenyl) were purchased from VWR analytical (BDH chemicals). Titanium (IV) n-butoxide (Ti[O(CH₂)₃]₄, 99+%) was purchased from Alfa Aesar. Ethanol Anhydrous 200 proof was purchase from Decon laboratories, Inc. Citric acid, anhydrous, powder and hydrochloric acid (36.5-38.0%) were purchased from J.T.Baker. Sodium borohydride ($\geq 99\%$) was purchased from Fluka Analytical.

Sodium tetrachloroaurate (III) dihydrate ($\geq 99\%$) and Rhodamine B (RhB) were purchased from Sigma-Aldrich. All chemicals and solvents were used as received.

B. Synthesis of TiO₂-nanosols

Titania nanosols was synthesized following a literature procedure.³⁶ In a 100 mL Erlenmeyer flask, 15.0 mL of absolute ethanol was added dropwise to 45.0 mL of Titanium (IV) n-butoxide with constant stir. The pH of the mixture was then adjusted to pH 2 using 37% hydrochloric acid (HCl), then stirred for forty-five minutes. The solution obtained was yellow (transparent) and homogeneous.

C. Pretreatment and Fabrication of CF@TiO₂ Substrate

One hundred percent white cotton fabric (CF) was cut into twelve square inches and pretreated for the fabrication process. Samples were pretreat using a non-ionic cleaning solution to deurate the fabric of any organic or inorganic compounds, grease, wax, and stains from its surface. To obtain the non-ionic cleaning solution, 5.000 g of sodium hydroxide (NaOH), 1.700 g of Triton X-100, and 0.758 g of citric acid was dissolved in 500.0 mL of DI water in a 1000 mL beaker. The solution was heated to 100.1°C, then one to five squares of the fabric was submerged into the solution for one hour. After the hour, samples were removed and rinsed with DI water serval times and dried at 42.1°C overnight. Treated CF (fig. 3.2A) was used during all fabricating process.

5.0 mL of TiO₂-nanosol was drop cast on each treated twelve square inches CF and dried at 72.1°C for three minutes, then cured at 42.1°C for twenty minutes to evaporate the ethanol solvent. Samples were then subjected to hydrothermal treatment by boiling on a hot plate for one hour at 80.1°C in a 100 mL Erlenmeyer flask. Samples were then dried at 42.1°C overnight. The fabricated CF@TiO₂ substrate was sonicated for thirty minutes to remove any unbounded TiO₂

particles, then dried at 42.1°C for one hour. The fabricated CF@TiO₂ substrate (fig. 3.2B) was stored in a weigh boat at room temperature.

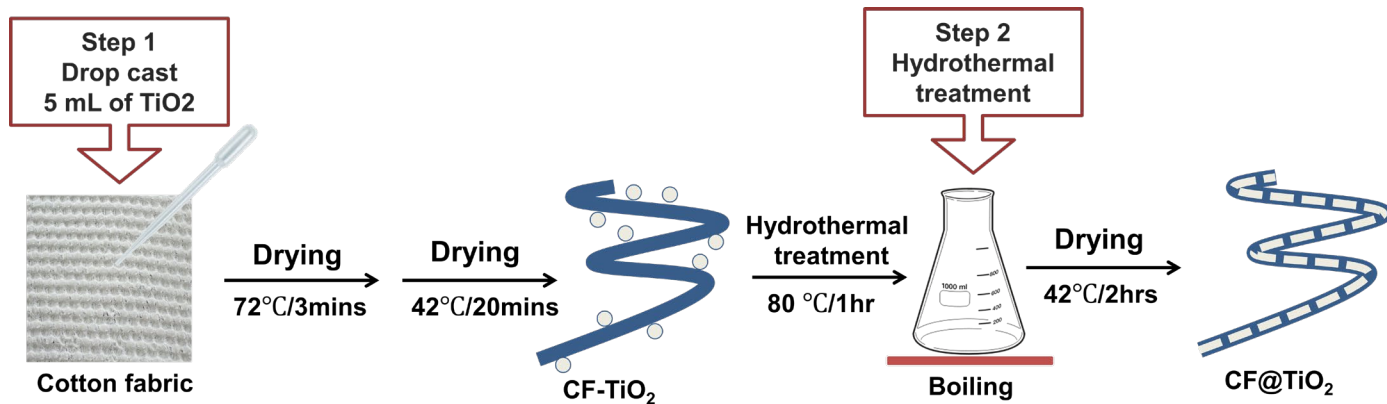


Figure 3.1. Process for the fabrication of CF@TiO₂ substrate.

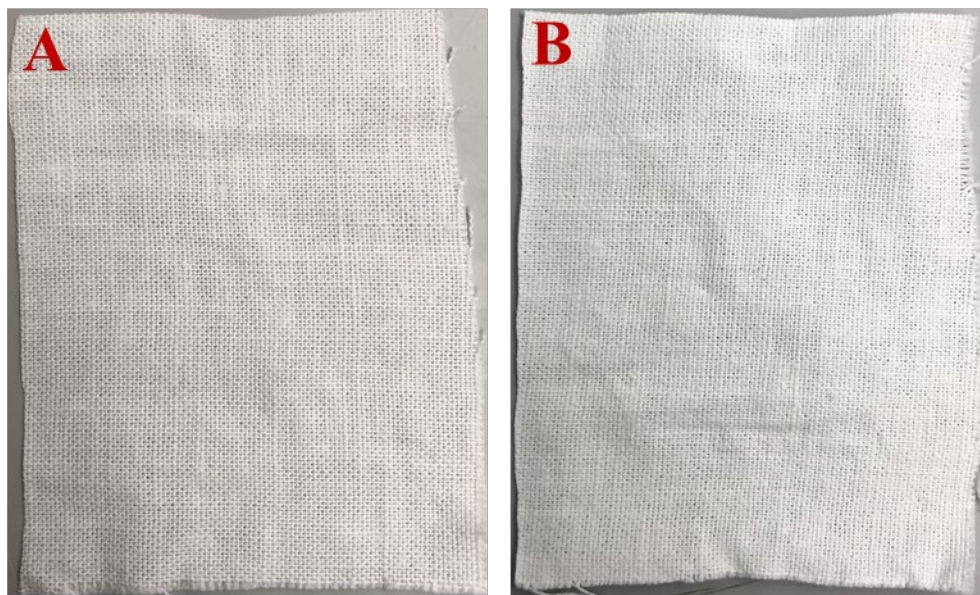
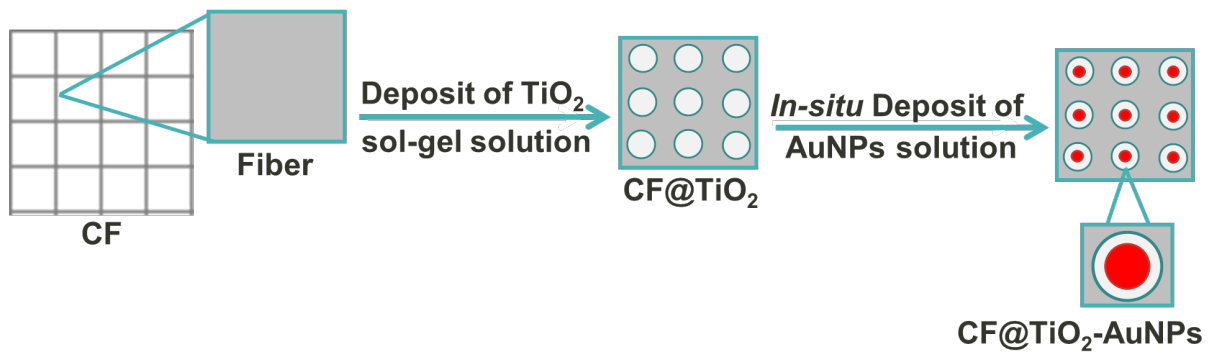


Figure 3.2. Digital photograph of A) pretreated cotton fabric and B) fabricated CF@TiO₂ substrate.

D. *In-situ* Deposition of Gold Nanoparticles

The fabricated CF@TiO₂ substrate was cut in to $2 \times 1\frac{1}{2}$ inches, then placed into a 50 mL beaker (used one at a time). CF@TiO₂-AuNPs composite material was prepared by adding 5.0 mL of 25 mM sodium tetrachloroaurate (III) dihydrate (NaAuCl₄) solution to the beaker and stand for five minutes to allow complete absorption of [AuCl₄]⁻ ions on to the surface of the TiO₂. The negatively charged [AuCl₄]⁻ adsorbs strongly on the positively charged surface of the TiO₂ nanoparticles. The NaAuCl₄ solution was discarded and the samples were rinsed several times with ethanol and DI water. The reduction of the [AuCl₄]⁻ ions was attained by the addition of 3.0 mL of 100 mM sodium borohydride (NaBH₄), a dark wine red color change was observed immediately on the fabric indicating the formation of AuNPs on the substrate. The NaBH₄ solution was discarded and the samples were rinsed several times with ethanol and DI water. CF@TiO₂-AuNPs composite material was dried at 42.1°C overnight and then stored in a weigh boat at room temperature. Scheme 3.2 illustrates the decoration of the TiO₂ semiconductor with AuNPs.



Scheme 3.2. Illustration of AuNPs on the surface of TiO₂.

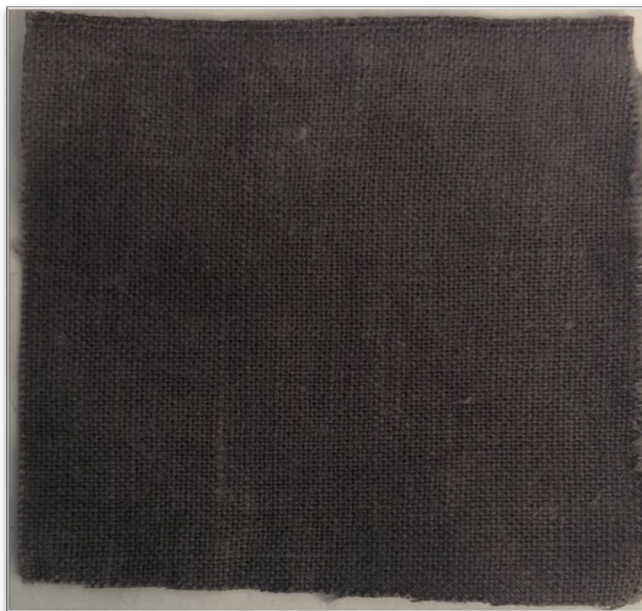


Figure 3.3. Digital photograph of CF@TiO₂-AuNPs composite material.

E. Characterization

XRD patterns of samples were collected using a Rigaku miniflex XRD system equipped with a D/Tex Ultra detector with a Cu target X-ray tube and a diffracted beam monochromator limiting the beam to Cu K α radiation at $\lambda = 1.5406 \text{ \AA}$. The generator was set for 40 kV and 15 mA. Data was collected between $2\theta = 5.0^\circ$ and 90.0° at 5.0° per minute. SEM-EDX was carried out on TESCAN VEGA3 SEM operating between 5.0 - 30.0 kV to which a ThermoFisher scientific UltraDry detector EDX system had been interfaced. All composite materials were cut into 0.5 cm and placed on an aluminum stub with carbon tape, then inserted into the SEM stage for analysis. Dye degradation in the presences of the photocatalyst was monitored using a Cary 4000 UV-visible spectrophotometer in the wavelength range from 280-700 nm, with a resolution of $<0.05 \text{ nm}$.

F. Photocatalytic Study

The photocatalytic degradation of aqueous RhB was carried out in a homemade 21 × 17 inches photocatalytic chamber equipped with a Black-Ray[®] XX-15BLB UV Bench Lamp (365 nm) and Reliable shaker (Model 55 Rocking shaker) to assess the photocatalytic activity of the binary system, CF@TiO₂-AuNPs. The study was done to monitor the change in RhB concentration versus the time of irradiation.

For the assessment, each composite material was cut into $\frac{1}{2} \times 1 \frac{1}{2}$ inches and affix to the side of a 4.5 mL polymethylmethacrylate (PMMA) cuvette, then 3.0 mL of 8 μM RhB was added. The cuvette was then sealed with a cap and parafilm to prevent leakage. A UV-Visible spectrum was collected at zero minutes for RhB and each composite material. Before irradiation, samples were sealed in a box on the shaker for thirty minutes to reach adsorption-desorption equilibrium. After thirty minutes dark, a UV-Visible spectrum was collected for each sample. For the UV irradiation study, samples were placed on the shaker three inches from the UV lamp. Once the chamber was sealed the light was turned on. A UV-Visible absorption spectrum for each sample was collected every ten minutes to monitor the decrease in RhB absorption maxima. When not in the chamber samples were kept in the dark box to limit visible light interaction.

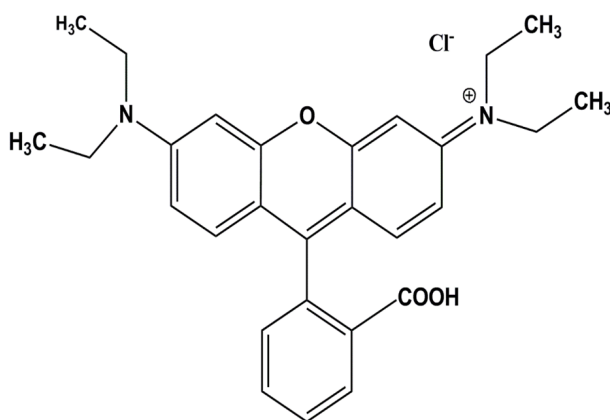


Figure 3.4. Molecular structure of Rhodamine B (RhB).

3.3 RESULTS AND DISCUSSION

For this project cotton fabric was coated with TiO₂ to generate a CF@TiO₂ substrate, then subsequently decorated with AuNPs to create a binary composite CF@TiO₂-AuNPs that has enhanced photocatalytic properties. The aim was to develop a simple, rapid, and reproducible binary system. Titanium (IV) n-butoxide was used as an inexpensive TiO₂ precursor with ethanol as a water-free reaction medium to fabricate TiO₂ thin layer on cotton fabric, a sol-gel method was used. Synthesis parameters such as deposition time, heating, cooling, and precursors volume to molar ratios were all important factors for the successful fabrication of a substrate. If the conditions of the synthetic method have not been fine-tuned the morphology of the resultant TiO₂ layer will show surface defects. Several different titania sol-gel methods were attempted to functionalize the surface of the fiber, however, this method yields the best results.

A. XRD Analysis

The XRD technique was used to determine the crystalline phase of the various composite materials, Figure 3.5 displays the XRD pattern for the unmodified CF, CF@AuNPs, and CF@TiO₂. The characteristic diffraction peaks observed at $2\theta = 14.4^\circ$, 16.2° , 22.6° , and 34.4° are distinctive peaks for cellulose I crystalline phase ((110), (110), (200) and (004)).³⁷ In CF@AuNPs nanocomposite a new peak appears at $2\theta = 37.8^\circ$ which represents the crystalline phase for AuNPs (1 1 1) plane. The presence of a single plane is related to the amount of AuNPs deposited on the surface of the CF. A study published by Das *et al.*, showed that the presences of a single plane (1 1 1) on the crystalline lattice of gold means there was approximately 2% of AuNPs loaded on a substrate.³⁸ Additional, characteristic diffraction peaks at $2\theta = 25.3^\circ$, 34.56° , 47.8° , and 54.5° are attributed to anatase TiO₂ which has (1 0 1), (0 0 4), (2 0 0), and (2 1 1) planes. The binary

composite showed an overlap broad distribution of the AuNPs (1 1 1) plane and the (0 0 4) plane of the anatase TiO₂ crystallite. The characterization data provided by the XRD confirmed the fabrication of the composite materials used in the binary system.

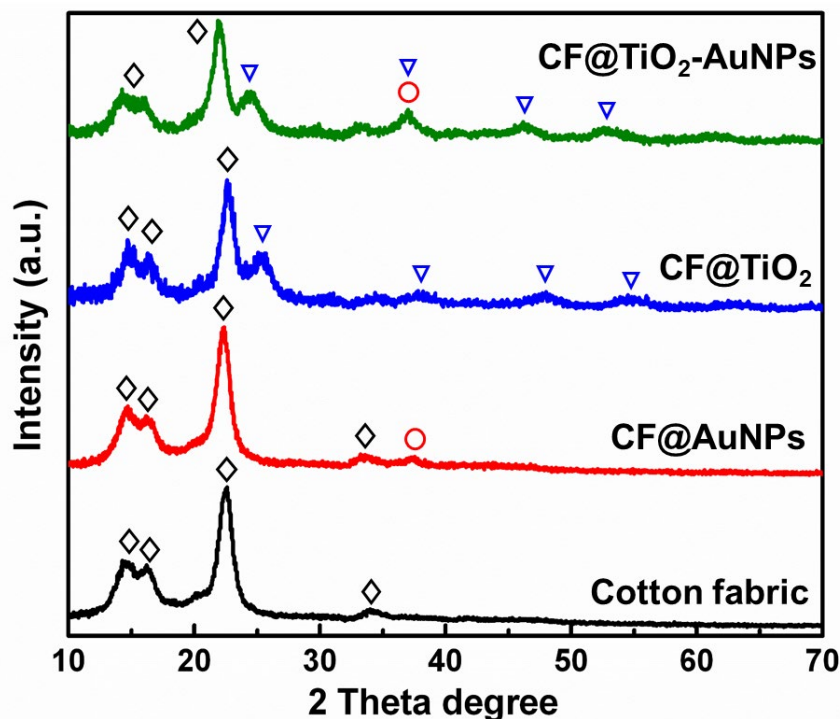


Figure 3.5. XRD patterns of the binary system samples: unmodified CF, CF@AuNPs, CF@TiO₂, and CF@TiO₂-AuNPs. The black diamond shape represents the diffraction pattern for CF, the red circle shape represents the diffraction pattern for AuNPs, and the blue triangle shape represents the diffraction pattern for TiO₂. XRD patterns for samples were collected using a Rigaku miniflex XRD system. Data was collected between $2\theta=5.0^\circ$ and 90.0° at 5.0° per minute.

B. SEM Images

The SEM images show the morphology of the TiO₂ thin layer used in the binary composite. Figure 3.6A illustrates the SEM image for unmodified CF. The SEM image of the surface showed that the fibers of the substrate are rather smooth. Next, figure 3.6B shows the surface topography of CF@TiO₂ nanocomposite, TiO₂ is attached by OH bonds to the surface of the fabric forming a thin film layer. Substantial cracks can be spotted on the surface of the thin film which is initiated

by synthesis conditions not being fine-tuned and possible surface tension which occurs during the curing process. The surface tensions could cause the thicker film, leading to a reduction of the bond strength between the semiconductor NPs.³⁵ Additionally, there could be a discrepancy of thermal expansion coefficient between the CF substrate and TiO₂ thin film.³⁹ Finally, figure 3.6C shows the morphology of CF@TiO₂-AuNPs nanocomposite, however, the in-house SEM could not be magnified into the nanometer ranger to get a closer visual of the NPs.

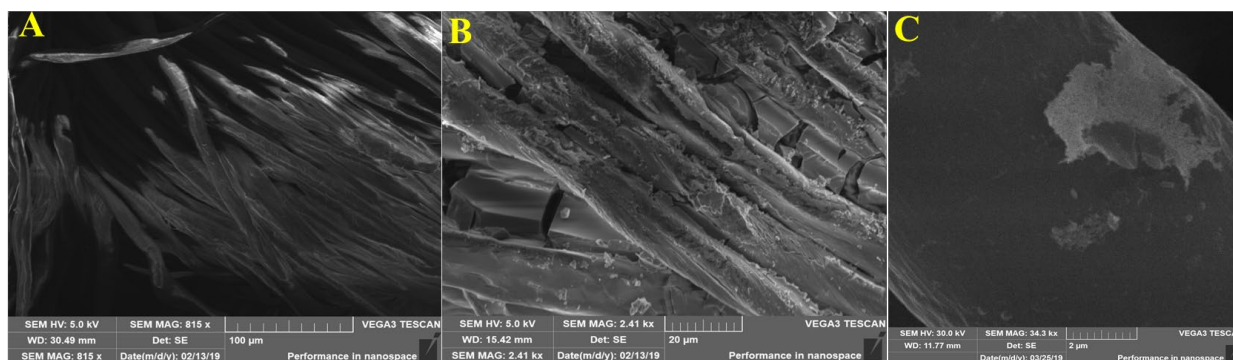


Figure 3.6. SEM images of the binary system samples: A) unmodified CF, B) CF@TiO₂, and C) CF@TiO₂-AuNPs. SEM was carried out on TESCAN VEGA3 SEM operating between 5.0 - 30.0 kV

C. EDX Line Analysis

SEM-EDX analysis was performed on the samples, and the technique was used to confirm and identify the elemental composition of the composite materials. Table 3.1 shows the EDX data for unmodified CF, CF@TiO₂, and CF@TiO₂-AuNPs nanocomposite. The unmodified CF showed peaks for carbon (C) and oxygen (O) with a weight percent of (33.73 C and 66.27 O) and atom percent of (40.41 C and 59.59 O). Appendix A.1 shows the reported EDX spectrum for cellulose fabric.⁴⁰ CF@TiO₂ nanocomposite showed three additional peaks (Appendix A.2), with the strongest at 0.6 keV whose weight percent was 40.90 and atom percent was 17.72. CF@TiO₂-AuNPs nanocomposite showed a weak peaks (Appendix A.3) for Au at 2 keV.⁴⁰ This is the reported peak for coating of gold on fabrics for SEM imaging.⁴⁰ The characterization images

provided by the SEM-EDX analysis confirmed the fabrication of the composite materials used in the binary system. EDX graphs are shown in **appendix A**.

Table 3.1. EDX line analysis data for binary composite. EDX graphs are shown in **appendix A**

Materials	Elements	Weight %	Atom %
CF	C K	33.73	40.41
	O K	66.27	59.59
		100	100
CF@TiO ₂	C K	13.01	22.48
	O K	44.09	59.79
	Ti K	--	--
	Ti L	40.90	17.72
		100	100
CF@TiO ₂ -AuNPs	C K	12.01	22.29
	O K	42.55	59.27
	Ti K	--	--
	Ti L	37.74	17.56
	Au M	7.70	0.87
		100	100

D. Photocatalytic Activity

The photocatalytic activity of CF@TiO₂-AuNPs was tested by assessing the photocatalytic degradation of aqueous RhB under UV irradiation. 8μM RhB (no composite), unmodified CF, and CF@TiO₂ were used as controls to compare the efficiency of the binary system. A system has active photocatalytic properties if there is a decrease in the concentration of aqueous RhB with the time of irradiation.

Figure 3.7A illustrates the UV-Visible absorption spectrum for 8μM RhB, the illumination in the presence of 8μM RhB (no composite) showed no changes in the adsorption spectrum indicating the absence of active photocatalytic properties without a composite material. The UV-Vis absorption spectrum for unmodified CF (Fig. 3.7B) showed a slight change after adsorption-desorption equilibrium (thirty minutes dark). However, illumination in the presence of

unmodified CF did not show the decrease in RhB absorption maxima indicating the absence of active photocatalytic properties. The absorption spectrum for CF@TiO₂ (Fig. 3.7C) is the first system that showed active photocatalytic properties. After adsorption-desorption equilibrium, there was a 28% decrease in RhB concentration, however, there was no change in the color of the solution. The illumination of CF@TiO₂ leads to an 87% decrease in the concentration of RhB within ninety minutes of UV irradiation along with changes to the color of the solution.

As noted in Figure 3.7C the spectrum show a hypsochromic shift (blue shift) of the RhB absorption band which could be correlated to the formation of a sequence of step-wise *N*-de-ethylated intermediates.⁴¹ This changes the rate of photodegradation of the dye and mechanistic pathway.⁴¹ For xanthene dyes such as RhB have *N*-alkylamine groups which may degrade through two pathways, first, the *N*-de-alkylation of the chromophore skeleton or second, the cleavage of the whole conjugated chromophore structure.⁴² Therefore, observing a blue shift indicates the formation of the *N*-de-ethylated intermediate which is caused by the destruction of the conjugated chromophore structure.⁴² Meaning that the backbone of the RhB structure was destroyed.⁴¹ The photoreactivity could also be hindered due to mineralization rate or type of photocatalyst used.⁴³ The photoreaction is prevented because a charge transfer is occurring between the excited RhB molecule and TiO₂ thin film. Therefore, surface interaction between the dye and semiconductor is restricted and the electrons cannot be injected from the excited RhB states into the conduction band of the TiO₂.⁴³

The absorption spectrum for CF@TiO₂-AuNPs (Fig. 3.7D) is the second system that showed active photocatalytic properties. After adsorption-desorption equilibrium, there was a 39% decrease in RhB concentration. However, there was no change in the color of the solution. The illumination of CF@TiO₂-AuNPs leads to a 94% decrease in the concentration of RhB within

ninety minutes of UV irradiation along with changes to the color of the solution. The observed changes indicated that light irradiation of CF@TiO₂-AuNPs composite in a photoreaction could lead to the degradation of aqueous RhB. From the study, we can infer that AuNPs is strongly related to the efficiency of the photocatalytic activity because it has high electron storage capacity and functions as a sink for the photoinduced charge carriers while promoting interfacial charge transfer process.³¹ Promoting robust interaction between Au and TiO₂ which increase the charge separation between the excited e^-_{CB} and h^+_{VB} enhancing the photocatalytic activity.³³

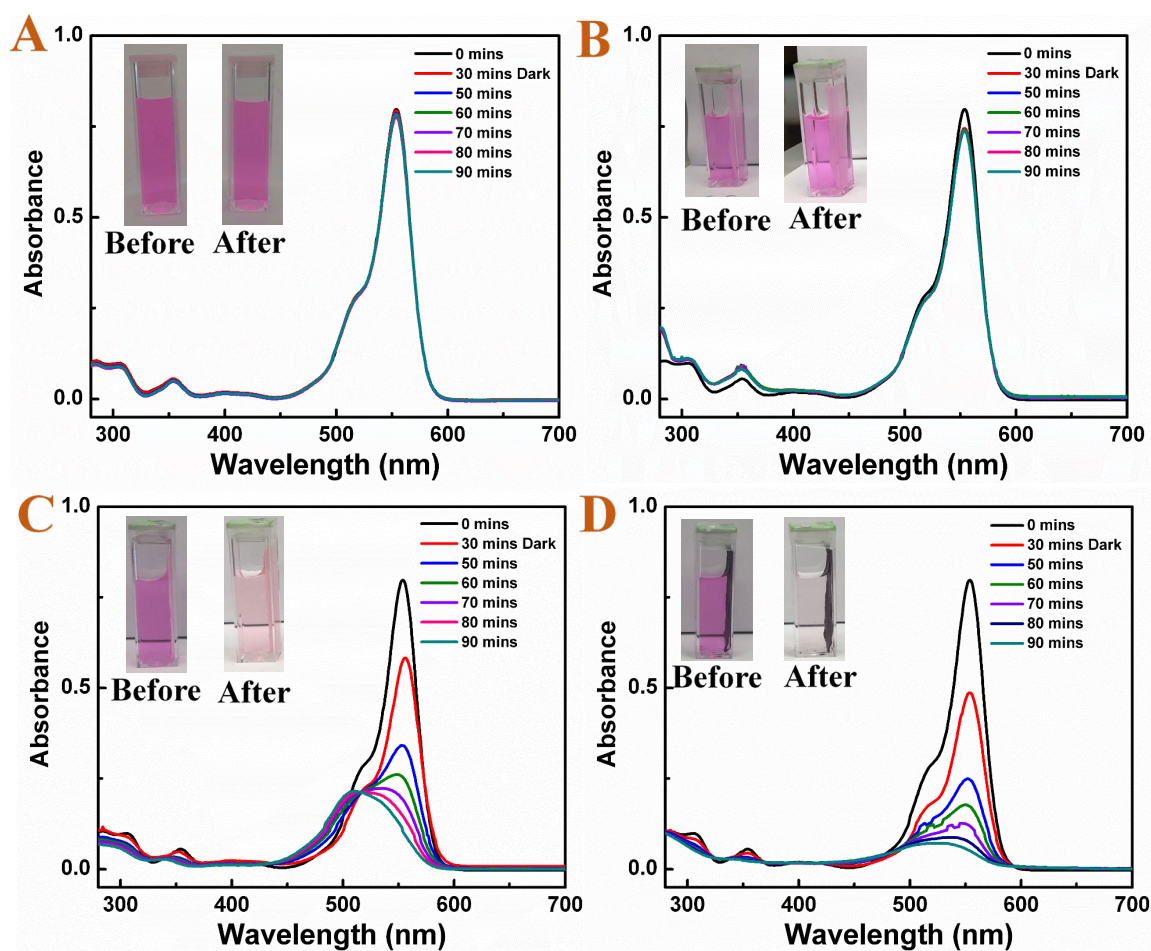


Figure 3.7. UV-Visible adsorption spectra of the photocatalytic degradation of 3.0 mL 8 μ M RhB under a UV light (365nm) in the presence of composite materials: (a) 8 μ M RhB (b) Cotton Fabric as a control, (c) CF@TiO₂ also as a control, (d) CF@TiO₂-AuNPs.

3.4 CONCLUSION

In this work, we fabricate CF@TiO₂ and CF@TiO₂-AuNPs nanocomposites. TiO₂ is first embedded in the cotton fabric following the solvothermal method. AuNPs were synthesized following *in-situ* method in the presence of CF@TiO₂ and thereby creating CF@TiO₂-AuNPs. XRD and SEM/EDX techniques characterized both the composites. We assessed these composite materials in degrading photocatalytic degradation of a RhB dye under UV irradiation. CF@TiO₂-AuNPs demonstrated significantly enhanced activity compared to CF@TiO₂.

CHAPTER 4. TERNARY SYSTEM

4.1 Ternary Composite

During the last few decades, TiO_2 and ZnO have received much attention for their applications as a semiconductors photocatalysis in wastewater treatment. Both are well studied semiconductors due to their low cost, quantum confinement,⁴⁴ non-toxicity, increase surface area,⁴⁴ chemical stability, and high photocatalytic activity. Both can yield photoinduced electron-hole pairs under UV irradiation which leads to an array of chemical redox reactions,⁴⁵ thus having the capability to decomposed and/or mineralized refractory organic or inorganic pollutants. ZnO and TiO_2 both have a wide band gap, therefore, restricting their photoinduced application to only under UV light. TiO_2 experience poor quantum yield because of its fast recombination of the photogenerated electron-hole pair and ZnO may experience imbalance chemical stoichiometry if not synthesized correctly causing degradation and chemical instability.⁴⁴ ZnO can also undergo photocorrosion at pH lower than 4.¹²

Thus, for them to make favorable photocatalysis they must have proper band alignment, morphology, and limited surface defects.⁴⁵ Therefore, to create better photocatalysis and improve their photoreactivity they can be used to develop heterogeneous structures for a binary system, as discussed in chapter 3, and ternary systems. In comparison to different core/shell nanomaterials binary composite ZnO-TiO_2 has been the most studied due to their limited difference in band gap energies, 3.2 eV for anatase TiO_2 and 3.3 eV for ZnO wurtzite. When combined there is a reduction in charge transfer rates and increase in photon conversion efficiencies which is attributed to the valence band of ZnO being located above the valence band and conduction band of TiO_2 which causes the photoinduced electron-hole pairs to separate within the system.⁴⁶ However, the electron-hole pair has a short lifespan, so the addition of a noble-metal NPs creates a more efficient system

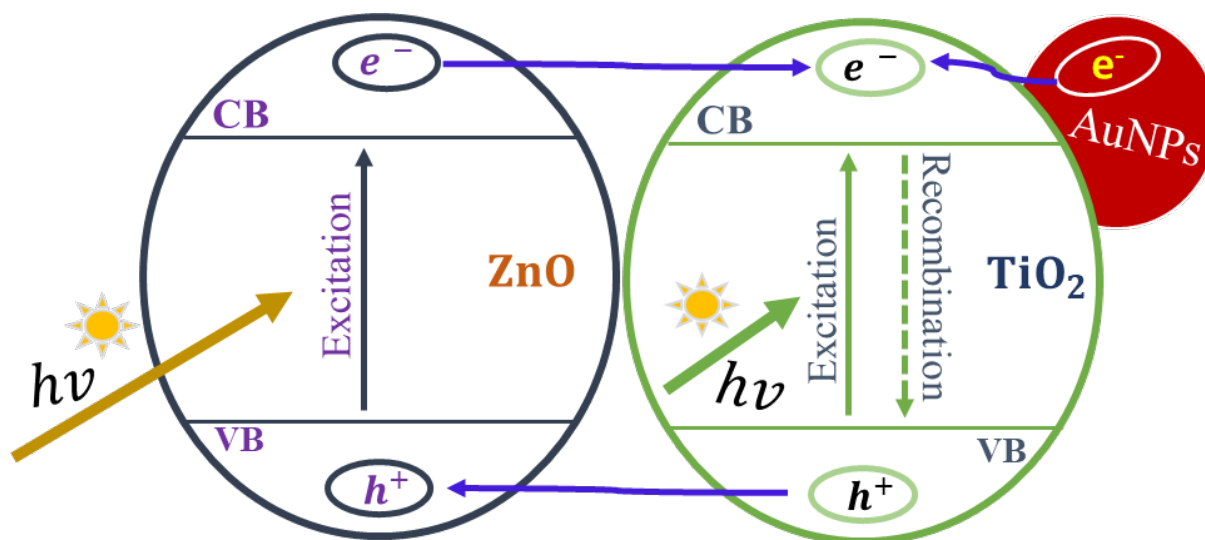
and further improve photocatalytic activity.⁴⁶ When the noble-metal NPs (e.g. Au) is added to the interfaces of ZnO-TiO₂ heterojunction it induces beneficial electrical and optical properties that improve the energy harvesting of the binary composite.⁴⁴

In comparison to the binary composite ZnO-TiO₂, the ternary composite ZnO-TiO₂-AuNPs should be superior due to the enhancement provided by the effects of the LSPR caused by visible light activation.⁴⁵ Along with the formation of the Schottky barrier at the TiO₂-AuNPs interface, with this barrier, the electrons are permanently transferred to the surface of Au and the holes are transmitted to the ZnO surface.⁴⁶ This phenomenon contributes to higher charge separation between the excited e^-_{CB} and h^+_{VB} enhancing the photocatalytic activity of the metal oxide.³³ When a metal interacts with a semiconductor a Schottky barrier occurs, the barrier is contributed to the electrons formed at the metal-semiconductor interface.⁴⁵

The ternary system has three mechanistic pathways which leads to favorable charge separation: (i) electrons being transferred from the conductance band of the TiO₂ to the Au due to the high Schottky barrier at the TiO₂-AuNPs interface causing a decrease in the recombination of the photogenerated electron-hole pair,^{45,46} (ii) electrons being transferred from the conductance band of the ZnO to the Au due to the Schottky barrier at the ZnO-AuNPs interface,^{45,46} (iii) small difference in wide band gaps promotes electron transfer from the conductance band of ZnO to conductance band of TiO₂ and holes in the valence band of TiO₂ could be trapped by the valence band of ZnO.^{45,46}

For this project, we fabricate CF@ZnONRs-TiO₂ and CF@ZnONRs-TiO₂-AuNPs heterogeneous structures for the degradation of RhB, to evaluate the efficiency of the nanocomposite when it is decorated with AuNPs. We hypothesized that CF@ZnONRs-TiO₂-AuNPs nanocomposite is a better system for the degradation of dye pollutants and should be more

efficient than the binary system due to the multiple degradation pathways. There should be no electron-hole recombination and enhanced photocatalytic activity in the ternary composite when compared to the binary composite CF@ZnO-TiO₂ due to the addition of the noble-metal NPs.



Scheme 4.1. Illustration of ZnO-TiO₂ and AuNPs interfacial charge transfer process.

4.2 MATERIALS AND METHODS

A. Materials

100% Cotton fabric used as a substrate, was purchased from a local Walmart. Sodium hydroxide beads, methanol, isopropyl alcohol (99%), and Triton X-100 (Polyethylene glycol tert-octylphenyl) were purchased from VWR analytical (BDH chemicals). Titanium (IV) *n*-butoxide (Ti [O(CH₂)₃]₄, 99+%), Ethylenediaminetetraacetic acid disodium salt dehydrate (EDTA-Na), and Benzoquinone (BQ) was purchased from Alfa Aesar. Ethanol Anhydrous 200 proof was purchase from Decon laboratories, Inc. Citric acid, anhydrous, powder, Zinc Nitrate, 6-hydrate crystals, and hydrochloric acid (36.5-38.0%) were purchased from J.T.Baker. Sodium borohydride (≥99%) was purchased from Fluka Analytical. Sodium tetrachloroaurate (III) dihydrate (≥99%) and Rhodamine B (RhB) were purchased from Sigma-Aldrich. Triethylamine (99%) was purchased from Acrōs

Organics. Zinc acetate, Buffer solution pH 2, Tert-butanol (T-BuOH), and hexamethylenetetramine were purchased from Fisher Scientific. All chemicals and solvents were used as received.

B. Synthesis of ZnO Seeds Solution

ZnO seed solution was synthesized following a literature procedure.⁴⁷ In a 100 mL round bottom three-neck flask, 1.100 g (5.0 mmol) of zinc acetate dihydrate was dissolved with 50.0 mL of isopropyl alcohol to make a 100 mM solution of zinc acetate dihydrate. The mixture was reflux for fifteen minutes at 85.1°C with constant stirring. After fifteen minutes, 700 μ L of trimethylamine (5.0 mmol) was added dropwise. Resulting in a cloudy solution, the mixture was then refluxed for an additional ten minutes at 85.1°C. Then, cooled to room temperature and incubated without stirring for three hours. The solution obtained was cloudy and used within three days.

C. Synthesis of ZnO Growth Solution

ZnO growth solution was synthesized following a literature procedure.⁴⁷ In a 300 mL beaker, 7.710 g of hexamethylenetetramine and 16.400 g of zinc nitrate were dissolved separately with 275.0 mL of DI water. Then, both solutions were combined in a 1000 mL Erlenmeyer flask and stirred at room temperature for twenty-four hours. The solution obtained was transparent. Creating a equimolar aqueous mixture of zinc nitrate hexahydrate and hexamethylenetetramine in order to grow ZnONRs on a substrate. ,

D. Synthesis of TiO₂-nanosols

TiO₂-nanosols were synthesized using the method described in Chapter 3.2 section B.

E. Synthesis of Radical Scavengers

In a 5 mL volumetric flask add 0.1861 g of EDTA-Na salt (100 mM) and dissolve in DI water. In a 5 mL volumetric flask add 0.0541 g of BQ (10 mM) and dissolve in methanol. In a 5 mL volumetric flask add 0.0371 g of T-BuOH (100 mM) and dissolve in DI water. All solutions were stored at room temperature.

F. Pretreatment

Cotton fabric was pretreated using the method described in Chapter 3.2 section C.

G. Fabrication of CF@ZnONRs-TiO₂ Substrate

To fabricate CF@ZnONRs substrate, five squares of the pretreated CF were first dip-coated in the ZnO seed solution for thirty minutes and then gently rinsed with ethanol. The dip-coated CF was then dried at 90.1°C for one hour and air dried at room temperature for twelve hours. At the end of the twelve hours, samples placed in an autoclave with 50.0 mL of the growth solution and incubated in a kiln at 90.1°C for eight hours. After, samples were removed from the autoclave and rinsed with DI water and allow to air dry at room temperature.

To fabricate CF@ZnONRs-TiO₂ substrate, the procedure described in Chapter 3.2 section C for CF@TiO₂ substrate fabrication was used.

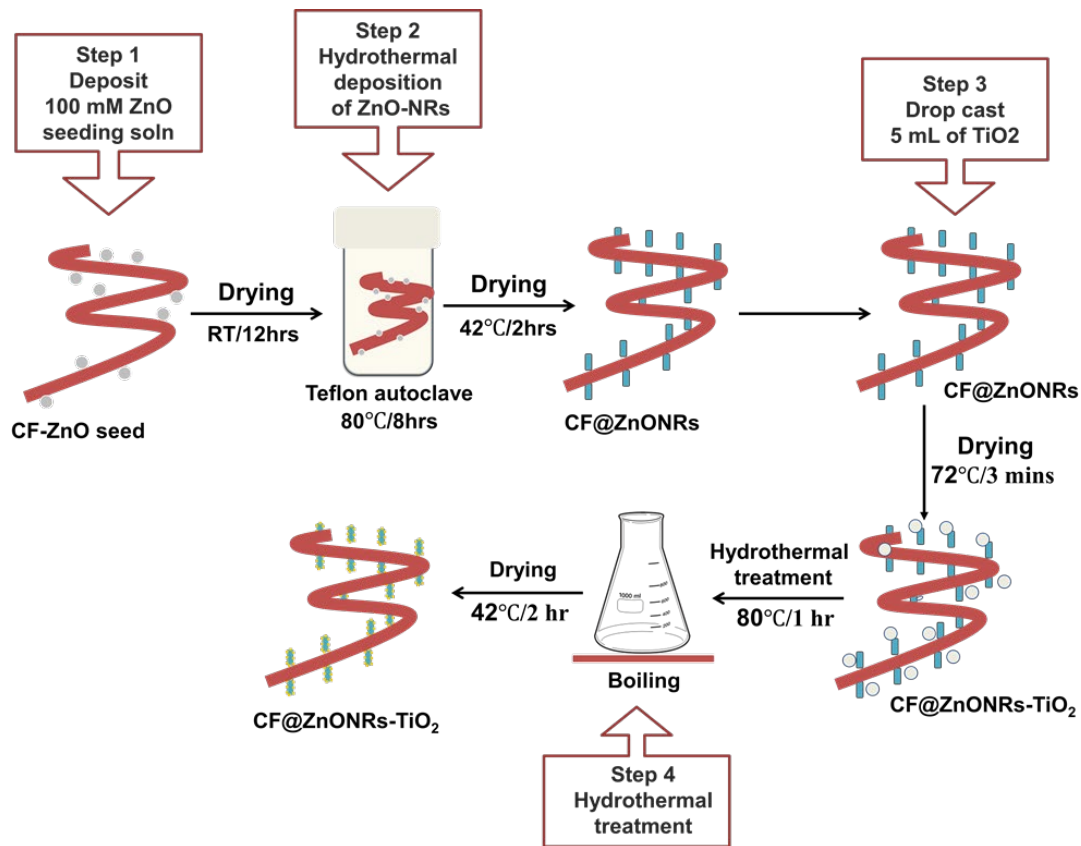


Figure 4.1. Process for the fabrication of CF@ZnONRs-TiO₂ substrate.

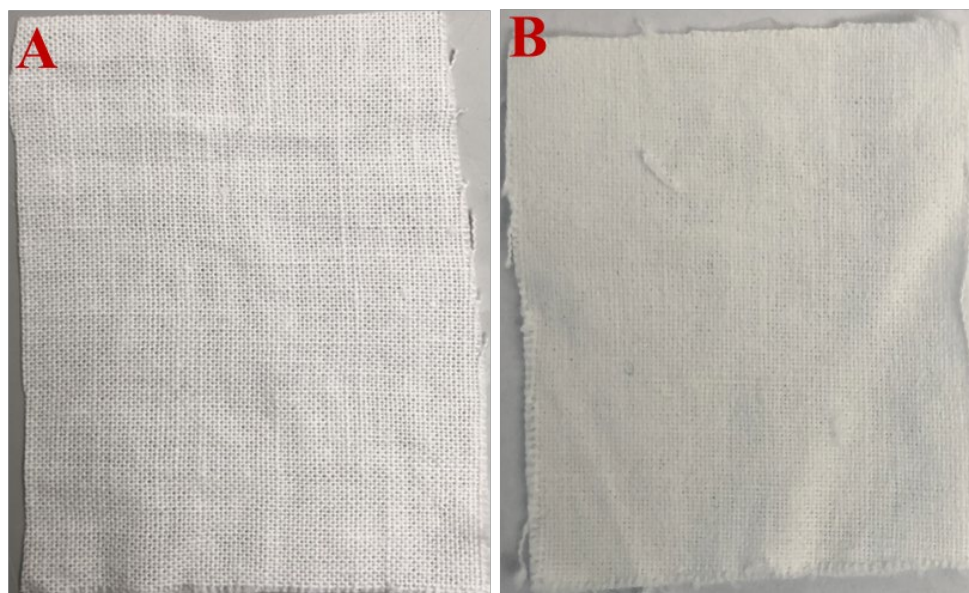
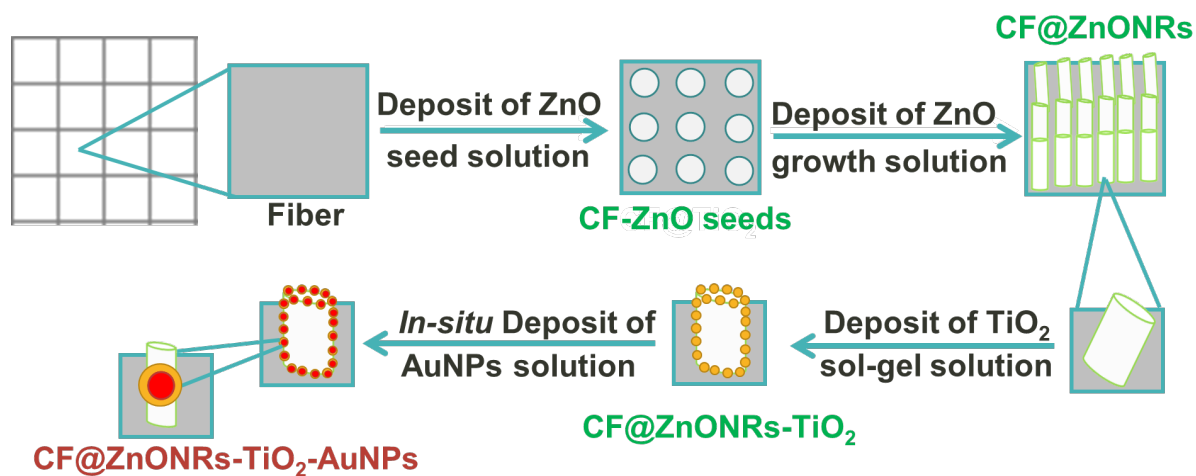


Figure 4.2. Digital photograph of A) pretreated cotton fabric and B) fabricated CF@ZnONRs-TiO₂ substrate.

H. *In-situ* Deposition of AuNPs

AuNPs were embedded on the CF@ZnONRs-TiO₂ substrate using the *in-situ* method described in Chapter 3.2 section D.



Scheme 4.2. Illustration of AuNPs on the surface of ZnONRsTiO₂.



Figure 4.3. Digital photograph of CF@ZnONRs-TiO₂-AuNPs composite material.

I. Characterization

The characterization instruments described in Chapter 3.2 section E was used for the ternary system characterization.

J. Photocatalytic Study

The photocatalytic study described in Chapter 3.2 section F was used to test the ternary system and conduct the recyclability study. However, for the radical trapping experiment the identical photocatalytic setup was used, however, 30 μL of each scavenger was add to the 3 mL of 8 μM RhB.

K. Gold Ion Leaching Experiment

In additional to the recyclability study, a gold ion leaching experiment was conducted to observe if gold ions were leaching from the composite material. For the experiment 3.0 mL of 8 μM RhB was degraded in the presence of CF@ZnONRs-TiO₂-AuNPs composite material for a hundred and twenty minutes. To four separate 1.5 mL centrifuge tube 500 μL of pH 2 buffer and 50 μL of 1 mM Benzidine was added. Then, 450 μL of unknown Au³⁺(solution from degradation), 450 μL of 10 μM of Au³⁺, and 450 μL of DI water was added to one of the 1.5 mL centrifuge tube and labeled. For each mixture a UV-visible absorption spectrum was collected.^{48,49}

4.3 RESULTS AND DISCUSSION

In addition to the binary nanocomposite discussed in chapter 3, a ternary nanocomposite was also fabricated. For the fabrication of the ternary system, cotton fabric was first coated with ZnONRs and characterized to confirm the presence of the ZnONRs thin layer on the fiber surface. The fabricated CF@ZnONRs substrate functioned as a core material for TiO₂ shell doping. Using the TiO₂ synthesis method developed in chapter two a binary composite of ZnONRs-TiO₂ core/shell nanostructure functionalized on the cotton fabric was generated. The binary composite

of CF@ ZnONRs-TiO₂ was then embedded with AuNPs to create a ternary system. The ternary composite is thought to have enhanced photocatalytic properties due to the addition of the noble-metal NPs which improves the energy harvesting capability of the modified composite.

A. XRD Analysis

The XRD patterns for the ternary composite is presented in figure 4.4, the patterns for unmodified cotton fabric, CF@AuNPs, CF@ZnONRs, CF@TiO₂, and CF@ZnONRs-TiO₂, and CF@ZnONRs-TiO₂-AuNPs are shown. The characteristic peaks at $2\theta = 14.4^\circ$, 16.2° , 22.6° , and 34.4° matches the reference pattern for cellulose I crystalline phase ((110), (110), (200) and (004)).³⁷ The addition reflection peak at $2\theta = 37.8^\circ$ corresponds to the (1 1 1) crystalline phase of AuNPs. As discussed in chapter 3, the appearance of only one crystalline phase is due to a low gold uptake. The characteristic reflection peaks that appears at $2\theta = 25.3^\circ$ (1 0 1), 34.56° (0 0 4), 47.8° (2 0 0), and 54.5° (2 1 1) are the diffraction peaks for anatase TiO₂. The reflection peaks at $2\theta = 31.75^\circ$, 34.42° , 36.24° , 47.53° , 56.57° , 62.85° , 66.34° , 67.92° , and 69.06° corresponding to (1 0 0), (0 0 2), (1 0 1), (1 0 2), (1 1 0), (1 0 3), (2 0 0), (1 1 2), and (2 0 1) planes which represents references pattern for wurtzite structures of ZnO. CF@ZnONRs-TiO₂ and CF@ZnONRs-TiO₂-AuNPs nanocomposite showed no new peaks which correlates to their reference pattern. There are multiple explanations as to why I was not able to get diffraction peaks for these samples.

The missing diffraction peaks could be related to the three-dimensional crystals not satisfying Bragg's conditions, the nanostructure of TiO₂ and ZnO are amorphous, and a limited amount of sample to quantify leading to lower intensity reflections making it challenging to detect from noise. Additionally, the sample could not be in crystalline phase because there is an appears for the cellulose I and AuNPs crystalline phase and the sample could also have less crystalline due

loss of a specific set of indices. The XRD technique could not confirm that I generated a ternary composite, therefore, I relied on the SEM/EDX data to confirm the present of ZnO, TiO₂ and AuNPs on the surface of the fiber.

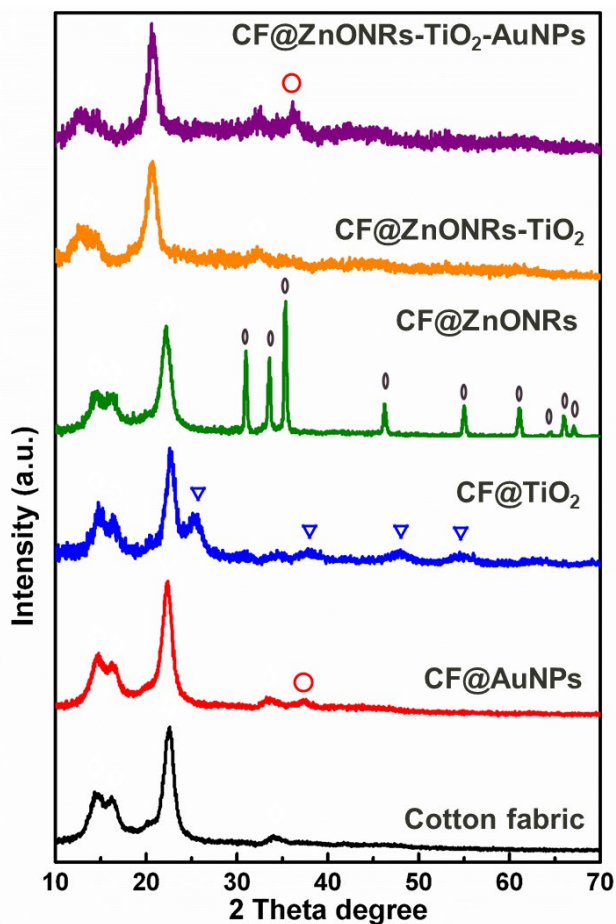


Figure 4.4. XRD patterns of the ternary system samples: unmodified CF, CF@AuNPs, CF@TiO₂, CF@ZnONRs, CF@ZnONRs-TiO₂-AuNPs. The black diamond shape represents the diffraction pattern for CF, the red circle shape represents the diffraction pattern for AuNPs, the blue triangle shape represents the diffraction pattern for TiO₂, and the green oval shape represents the diffraction pattern for CF@ZnONRs-TiO₂-AuNPs. XRD patterns for samples were collected using a Rigaku miniflex XRD system. Data was collected between $2\theta=5.0^\circ$ and 90.0° at 5.0° per minute.

B. SEM Images

The SEM images show the morphology of the ZnONRs and TiO₂ thin layer used in the ternary composite. Figure 4.5A illustrates the SEM image for unmodified CF. The SEM image of the surface showed that the fibers of the substrate are rather smooth. Figure 4.5B shows the SEM images for the cotton fabric functionalized with ZnONRs, and the high-resolution image showed an angularly aligned and dense deposition of ZnONRs coated on the fibers of the fabric. A closer magnification of the sample could not be obtained due to instrument magnification limitations of the in-house SEM. The SEM images for CF@ZnONRs-TiO₂ substrate is illustrated in figure 4.5C, from the data it was easily detected that surface deficiencies were present due to the synthesis method of TiO₂ not being fine-tuned as discussed in chapter 3. The SEM images from the ZnONRs showed uniform deposition, however, once coated with TiO₂ a dense layer filling the spaces between the fiber and nanorods is observed. Though ZnONRs can still be seen on some areas of the specimen, the joining layers of the ZnONRs and TiO₂ embody one compressed integument that has cracks. To rectify this issue further investigation is needed to optimize the deposition procedure of TiO₂. Finally, figure 4.5D shows the surface topography of CF@ZnONRs-TiO₂ AuNPs nanocomposite; however, the in-house SEM could not be magnified into the nanometer ranger to get a closer visual of the NPs.

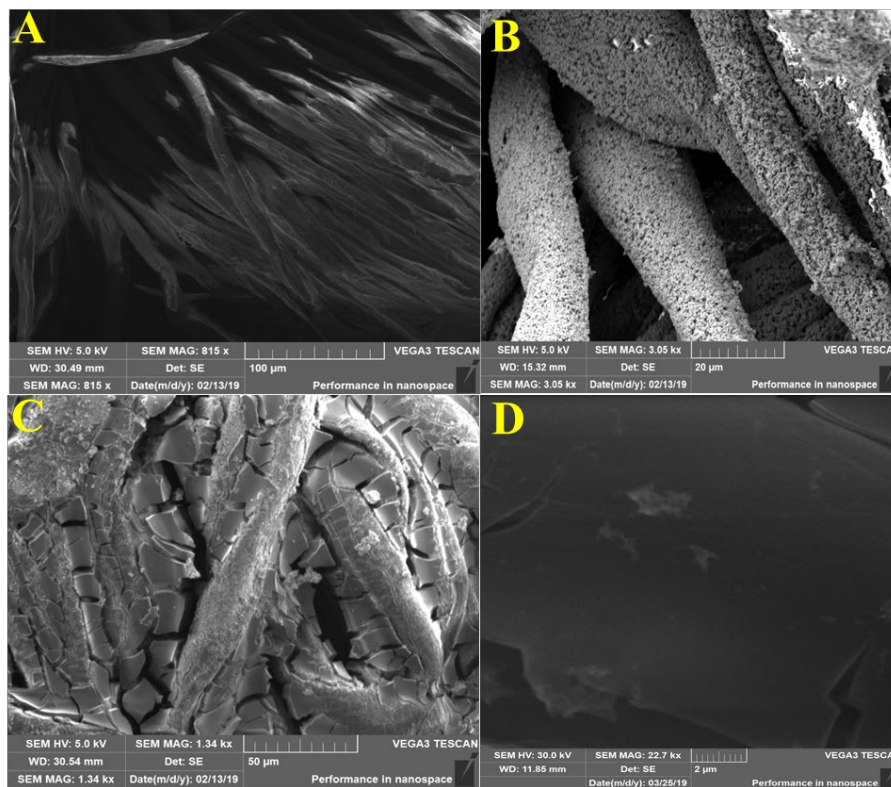


Figure 4.5. SEM images of the ternary system samples: A) unmodified CF, B) CF@ZnONRs, C) CF@ZnONRs-TiO₂, and D) CF@ZnONRs-TiO₂-AuNPs. SEM was carried out on TESCAN VEGA3 SEM operating between 5.0 - 30.0 kV

C. EDX line Analysis

SEM-EDX analysis was performed on the samples to identify the elemental composition of ZnO, TiO₂, and Au present in the composite materials. Table 4.1 shows the EDX data for unmodified CF, CF@TiO₂, CF@ZnONRs-TiO₂, and CF@ZnONRs-TiO₂-AuNPs nanocomposite. The unmodified CF showed peaks for carbon (C) and oxygen (O) with a weight percent of (33.73 C and 66.27 O) and atom percent of (40.41 C and 59.59 O). Correlating to the reported EDX spectrum for cellulose fabric.⁴⁰ CF@TiO₂ nanocomposite showed three new peaks, with the strongest at 0.6 keV whose weight percent was 40.90 and atom percent was 17.72. CF@ZnONRs nanocomposite showed two additional peaks (Appendix B.1), with the strongest at 1.0 keV whose weight percent was 81.38 and atom percent was 50.63. The EDX data for CF@ZnONRs-TiO₂

nanocomposite showed the presence of Ti (0.6 keV) and Zn (1.0 keV) ions in the specimen which correlates to the EDX spectrum for CF@ZnONRs-TiO₂ composites (Appendix B.2). This analysis confirmed the fabrication of the CF@ZnONRs-TiO₂ substrate. The weight percent for Zn and TiO₂ were 7.51 and 45.91 and the atom percent for Zn and TiO₂ were 2.76 and 23.05. The ternary composite showed the respected peaks for Ti and Zn ions plus a few shifted peaks for Au. This analysis confirmed the fabrication of the ternary composite CF@ZnONRs-TiO₂-AuNPs (Appendix B.3). The characterization images provided by the SEM-EDX analysis confirmed the fabrication of the composite materials used in the ternary system. EDX graphs are shown in **Appendix B**.

Table 4.1. EDX line analysis data for ternary composite. EDX graphs are shown in **appendix B**.

Materials	Elements	Weight %	Atom %
CF	C K	33.73	40.41
	O K	66.27	59.59
		<hr/> 100	<hr/> 100
CF@TiO ₂	C K	13.01	22.48
	O K	44.09	59.79
	Ti K	--	--
	Ti L	40.90	17.72
		<hr/> 100	<hr/> 100
CF@ZnONRs	C K	2.40	8.14
	O K	16.22	41.23
	Zn L	81.38	50.63
		<hr/> 100	<hr/> 100
CF@ZnONRS-TiO ₂	C K	8.30	16.62
	O K	38.29	57.56
	Ti K	--	--
	Ti L	45.91	23.05
	Zn L	7.51	2.76
		<hr/> 100	<hr/> 100
CF@ZnONRS-TiO ₂ -AuNPs	C K	10.42	20.59
	O K	38.22	56.74
	Ti K	--	--
	Ti L	39.71	19.69
	Zn L	6.50	2.36
	Au M	5.15	0.62
		<hr/> 100	<hr/> 100

D. Photocatalytic Activity

The photocatalytic activity for the ternary system was evaluated equivalently to the binary system. The ternary system CF@ZnONRs-TiO₂-AuNPs was tested to verify its photocatalytic properties, the assessment was done by analysis the photocatalytic degradation of aqueous RhB under UV irradiation. 8μM RhB (no composite), unmodified CF, and CF@ZnONRs-TiO₂ were used as controls to evaluate the effectiveness of the CF@ZnONRs-TiO₂-AuNPs composite material.

The UV-visible absorption spectrum for 8μM RhB (no composite) shown in figure 4.6A, the illumination in the presence of 8μM RhB (no composite) showed no changes in the adsorption spectrum indicating the absence of active photocatalytic properties without a composite material. The UV-Vis absorption spectrum for unmodified CF (Fig. 4.6B) showed a slight change after adsorption-desorption equilibrium (thirty minutes dark). However, illumination in the presence of unmodified CF did not show the decrease in RhB absorption maxima indicating the absence of active photocatalytic properties. The binary composite CF@ZnONRs-TiO₂ (Fig. 4.6C) showed active photocatalytic properties. However, there was also a blue shift. After thirty minutes in the dark, to formulate adsorption-desorption equilibrium, there was a 28% decrease in RhB with no significant changes to the color of the solution. The illumination of the composite lead to an 80% decrease in RhB concentration within ninety minutes of UV irradiation along with noticeable changes to the solution color.

As discussed in chapter 3 there are two pathways with which a xanthates dye can degrade, while the CF@TiO₂ substrate showed full cleavage of the whole chromophore structure in a series of step-wise intermediates, the binary composite of ZnO-TiO₂ only showed *N*-de-alkylation of the chromophore skeleton. The spectrum shows the full formation of the Rhodamine (498 nm)⁴³ *N*-

de-ethylation intermediate. However, the RhB absorption band is also present validating the degradation pathway. Figure 4.6D shows the absorption spectrum for CF@ZnONRs-TiO₂-AuNPs which shows active photocatalytic properties. After thirty minutes in the dark, to formulate adsorption-desorption equilibrium, there was a 33% decrease in RhB with no significant changes to the color of the solution. After illumination the ternary composite led to a 82% decrease in the concentration of RhB within ninety minutes of UV irradiation along with noticeable changes to the solution color. This result infers that the light irradiation of core/shell nanomaterials in a photoreaction can lead to the degradation of aqueous dye. From the study, it was concluded that the addition of AuNPs is strongly correlated to the high photocatalytic activity.

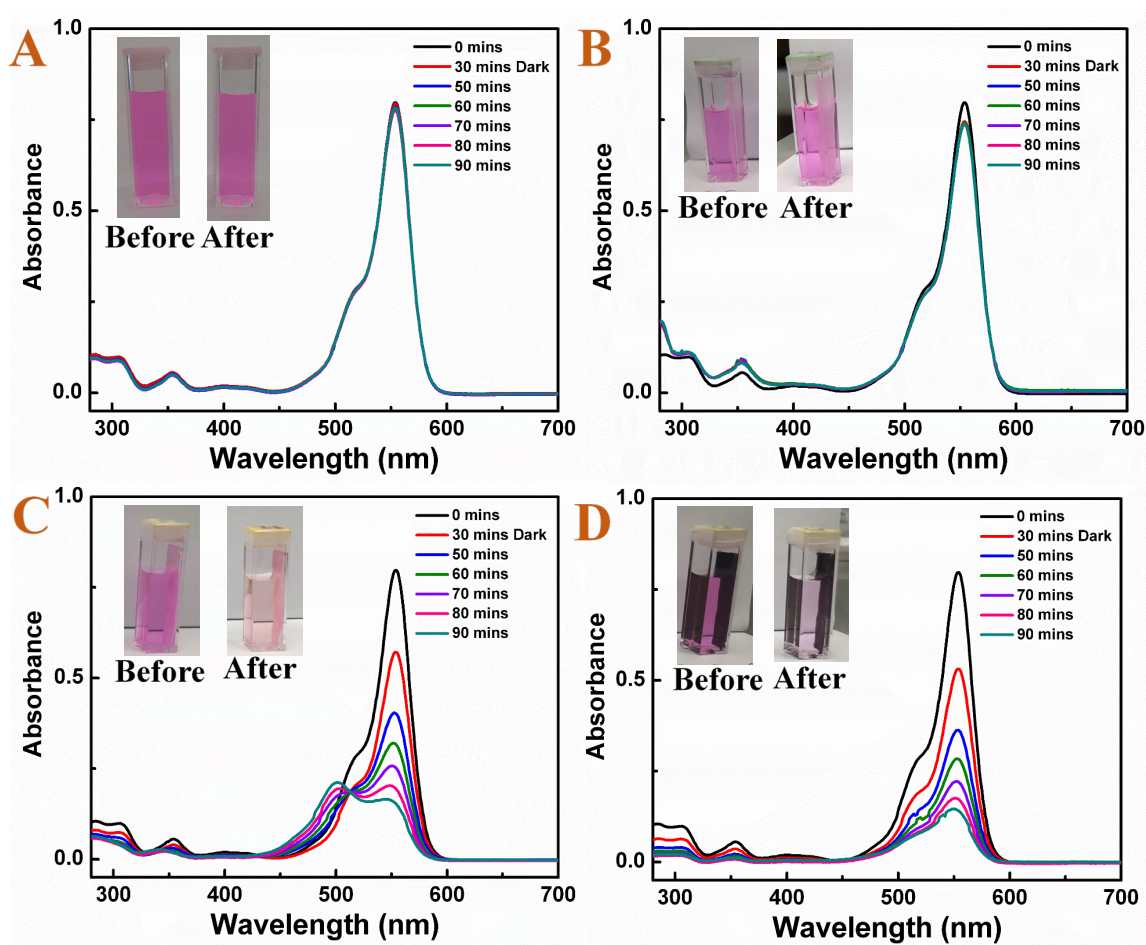


Figure 4.6. UV-Visible adsorption spectra of the photocatalytic degradation of 3.0 mL 8 μM RhB under a UV light (365nm) in the presence of composite materials: (a) 8 μM RhB (b) Cotton Fabric as a control, (c) CF@ZnONRs-TiO₂ also as a control, (d) CF@ZnONRs-TiO₂-AuNPs.

E. Gold Leaching Experiment

The photocatalytic data from the binary and ternary system were compared and the nanocomposite with the best photocatalytic data was chosen to run a gold leaching experiment to monitor if gold ions were leaching from the composite material. Figure 4.7 shows the UV-Visible adsorption spectrum for the study. Due to the absence of a absorption band at 425 nm for the composite material it was infer that gold ions were not leaching from the nanocomposite.

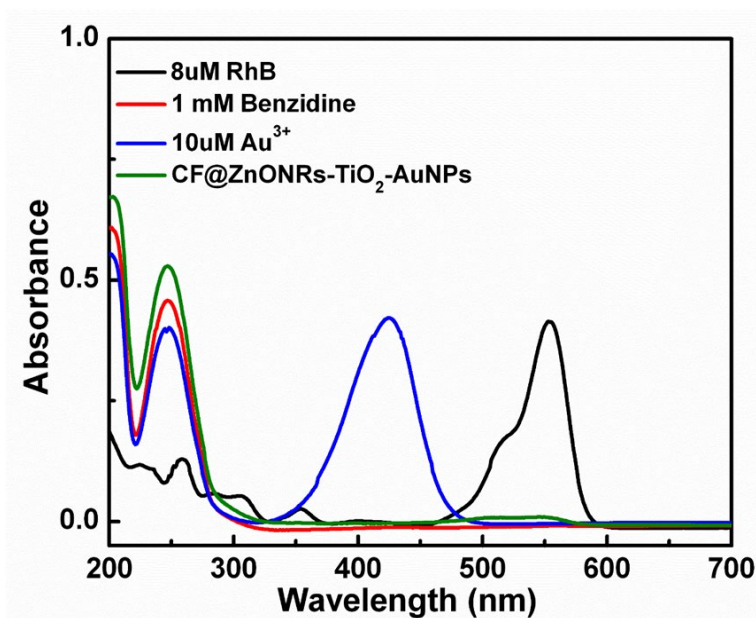


Figure 4.7. UV-Vis adsorption spectrum for gold ion leaching experiment. The photocatalytic degradation of 3.0 mL 8 μ M RhB under a UV light (365nm) in the presence of CF@ZnONRs-TiO₂-AuNPs.

F. Radical Trapping of Ternary Nanocomposite

Using the ternary composite material a radical trapping study was conducted to observe the photocatalytic mechanism and to understand which radical is the active oxidative species for the degradation of the dye pollutant. EDTA was used for the h^+ , BQ was used for the $O_2^{\cdot-}$ radical, and T-BuOH was used for the OH^{\cdot} radical. The scavengers were added to the photocatalytic reaction for 8 μ M RhB under UV irradiation to monitor the oxidative species during the irradiation in the presences of CF@ZnONRs-TiO₂-AuNPs nanocomposite. The results of the study are shown in figure 4.8. If EDTA or T-BuOH was added to the reaction the rate of the photocatalytic degradation of RhB was not affected when compared to the composite material data, the data even showed the reaction going faster than the composite material, which leads to the assumption that maybe there was charge-transfer recombination occurring. This suggested that the h^+ and OH^{\cdot} radical were not the main oxidative species driving the photocatalytic process. However, when BQ was added withholding the $O_2^{\cdot-}$ radical there was a significant decrease in the photocatalytic degradation of RhB suggesting that the $O_2^{\cdot-}$ radical is the active oxidative species used in the photocatalytic process.

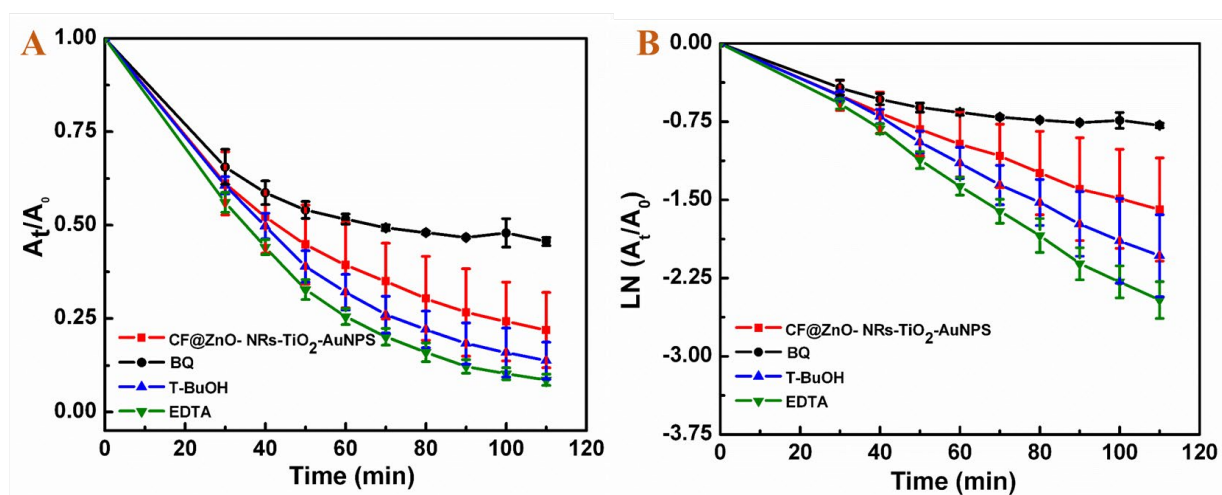


Figure 4.8. The photocatalytic degradation of 3.0 mL 8 μ M RhB under a UV light (365nm) in the presence of CF@ZnONRs-TiO₂-AuNPs, with (green, blue, black) and without (red) radical scavengers.

4.4 CONCLUSION

In this work we fabricate CF@ZnONRs-TiO₂ and CF@ZnONRs-TiO₂-AuNPs nanocomposite for the degradation of aqueous RhB, to evaluate the efficiency of the nanocomposite when it is decorated with AuNPs. Then the binary and ternary composite material photocatalytic degradation data were compared, the system with the best results were used to conduct recyclability and radical trapping study to test the recoverability and reusability of the nanocomposite. While the radical trapping experiment was done to observe which oxidative species is the main radical responsible for the photocatalytic process. I was able to fabricate CF@ZnONRs and CF@ZnONRs-TiO₂ substrate successfully, then decorate the fabricated substrate (CF@ZnONRs-TiO₂) with AuNPs. The composite material were characterized by XRD and SEM/EDX. The ternary system was successfully created and the composite material was shown to be capable of photocatalyzing the degradation of a dye under UV irradiation and showed enhanced photocatalytic performance in the presence of AuNPs. The radical trapping experiment indicating that the $O_2^{\cdot -}$ radical is the primary active oxidative species in the photodegradation of the dye.

References

1. Malhotra, B. D.; Ali, M. A. Chapter 3 - Bioconjugated Nanostructured Metals and Metal Oxides for Biosensors. In *Nanomaterials for Biosensors*; Malhotra, B. D., Ali, M. A., Eds.; William Andrew Publishing: 2018; pp 105-125.
2. Thomas, K. G.; Kamat, P. V. Chromophore-Functionalized Gold Nanoparticles. *Acc. Chem. Res.*, **2003**, *36*, 888-898.
3. Costa, A. L.; Ortelli, S.; Blosi, M.; Albonetti, S.; Vaccari, A.; Dondi, M. TiO₂ based photocatalytic coatings: From nanostructure to functional properties. *Chem. Eng. J.*, **2013**, *225*, 880-886.
4. Bhatkhande, D. S.; Pangarkar, V. G.; Beenackers, A. A. Photocatalytic degradation for environmental applications – a review. *J. Chem. Technol. & Biotechnol.*, **2002**, *77*, 102-116.
5. Saad, R. S.; Mahmed, N.; Abdullah, M. M.; Sandu, V. A. Self-Cleaning Technology in Fabric: A Review. *IOP Conf. Ser.: Mater. Sci. Eng.*, **2016**, *133*, 012028.
6. Dagherir, R.; Drogui, P.; Robert, D. Modified TiO₂ for Environmental Photocatalytic Applications: A Review. *Ind. Eng. Chem. Res.*, **2013**, *52*, 10, 3581-3599.
7. Macwan, D. P.; Dave, P. N.; Chaturvedi, S. A review on nano-TiO₂ sol-gel type syntheses and its applications. *J. Mater. Sci.*, **2011**, *46*, 3669.
8. Pelaez, M.; Nolan, N. T.; Pillai, S. C.; Seery, M. K.; Falaras, P.; Kontos, A. G.; Dunlop, P. S. M.; Hamilton, J. W. J.; Byrne, J. A.; O'Shea, K.; Entezari, M. H.; Dionysiou, D. D. A review on the visible light active titanium dioxide photocatalysts for environmental applications. *Appl. Catal. B-Environ.*, **2012**, *125*, 331-349.
9. Dawson, A.; Kamat, P. V. Semiconductor-metal nanocomposites. Photoinduced fusion and photocatalysis of gold-capped TiO₂. *J. Phys. Chem. B*, **2001**, *105*, 960.
10. Fageria, P.; Gangopadhyay, S.; Pande, S. Synthesis of ZnO/Au and ZnO/Ag nanoparticles and their photocatalytic application using UV and visible light. *RSC Adv.*, **2014**, *4*, 24962-24972.
11. Kołodziejczak-Radzimska, A.; Jesionowski, T. Zinc Oxide—From Synthesis to Application: A Review. *Materials*, **2014**, *7*, 2833-2881.

12. Chen, C.; Fan, H.; Jan, J. Degradation Pathways and Efficiencies of Acid Blue 1 by Photocatalytic Reaction with ZnO Nanopowder. *J. Phys. Chem. C*, **2008**, *112*, 11962-11972.
13. Sirelkhatim, A.; Mahmud, S.; Seeni, A.; Kaus, N. H. M.; Ann, L. C.; Bakhori, S. K. M.; Hasan, H.; Mohamad, D. Review on Zinc Oxide Nanoparticles: Antibacterial Activity and Toxicity Mechanism. *Nanomicro. Lett.*, **2015**, *7*, 219-242.
14. Wang, L. Z. Zinc oxide nanostructures: growth, properties and applications. *J. Phys.: Condens. Matter*, **2004**, *16*, R829–R858.
15. Abid, M.; Bouattour, S.; Ferraria, A. M.; Conceição, D. S.; Carapeto, A. P.; Vieira Ferreira, L. F.; Botelho do Rego, A. M.; Rei Vilar, M.; Boufi, S. Functionalization of cotton fabrics with plasmonic photo-active nanostructured Au-TiO₂ layer. *Carbohydr. Polym.*, **2017**, *176*, 336-344.
16. Linley, S.; Lui, Y. Y.; Ptacek, C. J.; Blowes, D. W.; Gu, F. X. Recyclable Graphene Oxide-Supported Titanium Dioxide Photocatalysts with Tunable Properties. *Appl. Mater. Interf.*, **2014**, *6*, 4658–4668.
17. Jiang, Z.; Jiang, D.; Yan, J. Z.; Liu, D.; Qian, K. Xie, J. A new visible light active multifunctional ternary composite based on TiO₂-In₂O₃ nanocrystals heterojunction decorated porous graphitic carbon nitride for photocatalytic treatment of hazardous pollutant and H₂ evolution. *Appl. Catal. B: Environ.*, **2015**, *170*, 195-205.
18. Yang, Y.; Xu, M. L.; Wang, H.; Fu, N. , Preparation of reduced graphene oxide/meso-TiO₂/AuNPs ternary composites and their visible-light-induced photocatalytic degradation of methylene blue. *App. Surf. Sci.*, **2016**, *369*, 576-583.
19. Bunaciu, A. A.; Udriștioiu, G. E.; Aboul-Enein, Y. H. X-Ray Diffraction: Instrumentation and Applications. *Critical Reviews in Analytical Chemistry*, **2015**, *4*, 289-299.
20. Chauhan, A.; Chauhan, P. Powder XRD Technique and its Applications in Science and Technology. *J. Anal. Bioanal. Tech.*, **2014**, *5*, 212.
21. Eckert, M. Max von Laue and the discovery of X-ray diffraction in 1912. *Ann. Phys. (Berlin)*, **2012**, *524*, A83–A85.
22. Inaba, K.; Kobayashi, S.; Uehara, K.; Okada, A. High Resolution X-Ray Diffraction Analyses of (La,Sr)MnO₃/ZnO/Sapphire (0001) Double Heteroepitaxial Films. *Advances in Materials Physics and Chemistry*, **2013**, *3*, 72-89.

23. Jany, B. R.; Janas, A.; Krok, F. Retrieving the Quantitative Chemical Information at Nanoscale from Scanning Electron Microscope Energy Dispersive X-ray Measurements by Machine Learning. *Nano. Lett.*, **2017**, *17*, 6520-6525.
24. Burgess, Simon, et al. "High Spatial Resolution Energy Dispersive X-Ray Spectrometry in the SEM and the Detection of Light Elements Including Lithium." *Microscopy and Analysis*, May 2013, pp. S8–S13.
25. "Why Use SEM?" Scientific overview. - Orsay Physics, www.orsayphysics.com/what-is-sem.
26. Perkampus, H.; Grinter, H.; Threlfall, T. L. UV-VIS Spectroscopy and its Applications. *Springer*, **1992**, pp 1-9.
27. *New Discovery Could Stimulate Plant Growth and Increase Crop Yields - Durham University*, www.dur.ac.uk/chemistry/outreach/spectroscopy_in_a_suitcase/absorption_spectroscopy/.
28. Choudhary, A.; "The Principle of Ultra Violet (UV) Spectrophotometer." *Medium.com*, Medium, 12 Oct. 2017, medium.com/@ankur1857/principle-of-ultra-violet-uv-spectrophotometer-e6a1c435d258.
29. Howell, J. A.; Sutton, R. E. Ultraviolet and Absorption Light Spectrometry. *Anal. Chem.*, **1998**, *70*, 118.
30. Sobarwiki, 2 September 2013, <http://www.wikipedia.org/>.
31. Corella, D. A., and Baruah, B. "3D macroporous TiO₂ inverse opal binary and ternary composite materials and their photocatalytic activity." *RSC. Adv.*, **2017**, *7*, 47038–47048.
32. Devi, L. G.; Kavitha, R. A review on non-metal ion doped titania for the photocatalytic degradation of organic pollutants under UV/solar light: Role of photogenerated charge carrier dynamics in enhancing the activity. *Appl. Catal, B-Environ.*, **2013**, *140-141*, 559-587.
33. Ayati, A.; Ahmadpour, A.; Bamoharram, F. F.; Tanhaei, B.; Mänttari, M.; Sillanpää, M. A review on catalytic applications of Au/TiO₂ nanoparticles in the removal of water pollutant. *Chemosphere*, **2014**, *107*, 163-174.
34. Lu, Y.; Yu, H.; Chen, S.; Quan, X.; Zhao, H. Integrating Plasmonic Nanoparticles with TiO₂ Photonic Crystal for Enhancement of Visible-Light-Driven Photocatalysis. *Environ. Sci. Technol.*, **2012**, *46*, 1724-1730.

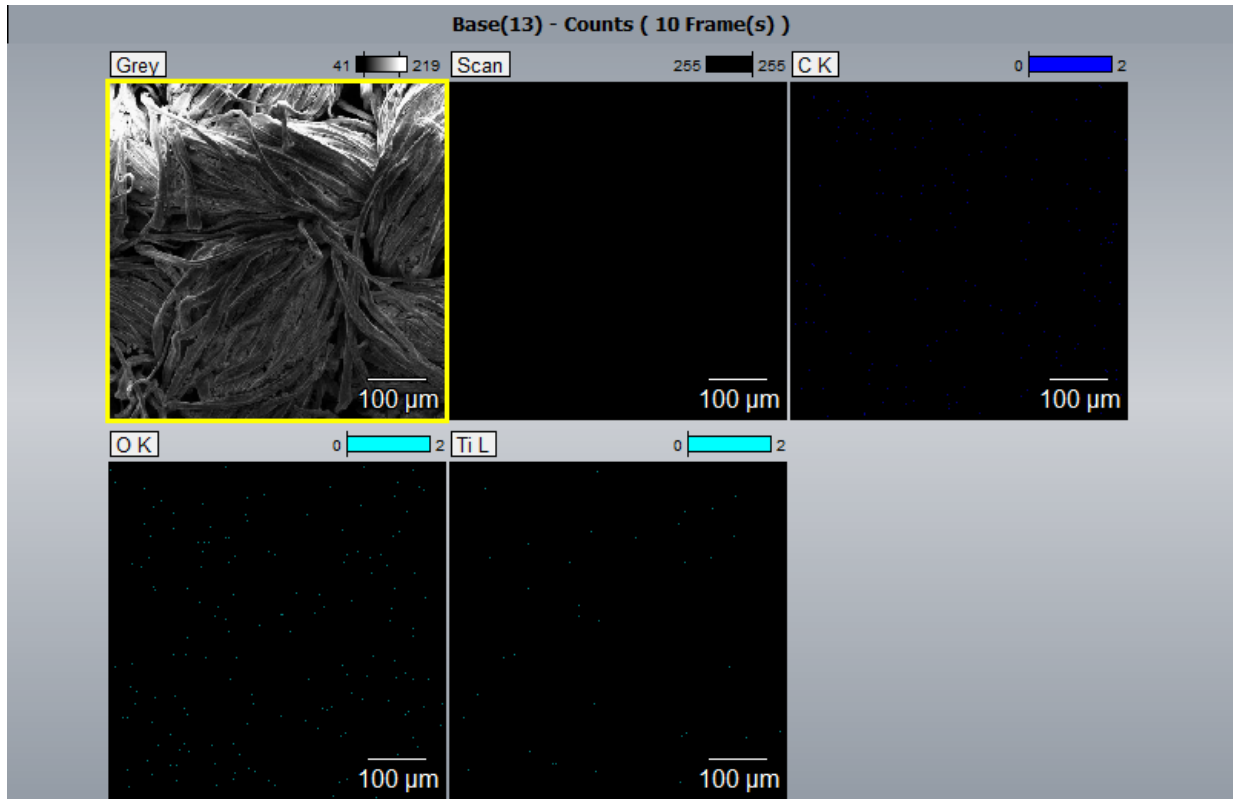
35. Julkapli, N. M.; Bagheri, S.; Abdullah, F. Z. Photocatalytic activities and photoinduced fusion of gold-modified titania nanoparticle. *Rev. Inorg. Chem.*, **2017**, *37*, 95–103.
36. Abid, M.; Bouattour, S.; Ferraria, A. M.; Conceição, D. S.; Carapeto, A. P. Functionalization of cotton fabrics with plasmonic photo-active nanostructured Au-TiO₂ layer. *Carbohydr. Res.*, **2017**, *176*, 336-344.
37. Morawski, A.W.; Kusiak-Nejman, E.; Przepiórski, J. Cellulose-TiO₂ nanocomposite with enhanced UV–Vis light absorption. *Cellulose*. **2013**, *20*, 1293.
38. Das, R. K.; Borthakur, B. B.; Bora, U. Green synthesis of gold nanoparticles using ethanolic leaf extract of *Centella asiatica*. *Mater. Lett.* **2010**, *64*, 1445-1447.
39. Meen, T.; Tsai, J.; Tu, Y.; Wu, T.; Hsu, W.; Chang, S. Optimization of the dye-sensitized solar cell performance by mechanical compression. *Nanoscale Res. Lett.* **2014**, *9*, 1-8.
40. Yazdanshenas, M. E.; Shateri-Khalilabad, M. In situ synthesis of silver nanoparticles on alkali-treated cotton fabrics. *J. IND. TEXT.* **2013**, *42*, 459-474.
41. Fu, H.; Pan, C.; Yao, W.; Zhu, Y. Visible-Light-Induced Degradation of Rhodamine B by Nanosized Bi₂WO₆. *J. Phys. Chem. B.* **2005**, *109*, 22432-22439.
42. Chen, C.; Zhao, W.; Li, J.; Zhao, J.; Hidaka, H.; Serpone, N. Formation and Identification of Intermediates in the Visible-Light-Assisted Photodegradation of Sulforhodamine-B Dye in Aqueous TiO₂ Dispersion. *Environ. Sci. Technol.* **2002**, *36*, 3604-3611.
43. Fu, H.; Zhang, S.; Xu, T.; Zhu, Y.; Chen, J. Photocatalytic Degradation of RhB by Fluorinated Bi₂WO₆ and Distributions of the Intermediate Products. *Environ. Sci. Technol.* **2008**, *42*, 2085-2091.
44. Javed, F.; Javed, S.; Akram, M. A.; Mujahid, M.; Islam, M.; Bhatti, A. S. Surface plasmon mediated optical properties of ZnO/Au/TiO₂ nanoheterostructure rod arrays. *Mater. Sci. Eng., B*, **2018**, *231*, 32-39.
45. Mukhopadhyay, S.; Maiti, D.; Chatterjee, S.; Devi, P. P.; Kumar, G. S. Design and application of Au decorated ZnO/TiO₂ as a stable photocatalyst for wide spectral coverage. *Phys. Chem. Chem. Phys.*, **2016**, *18*, 31622-31633.
46. Zhang, P.; Shao, C.; Li, X.; Zhang, M.; Zhang, X.; Sun, Y.; Liu, Y. In situ assembly of well-dispersed Au nanoparticles on TiO₂/ZnO nanofibers: A three-way synergistic heterostructure with enhanced photocatalytic activity. *J. Hazard. Mater.*, **2012**, *237-238*, 331-338.
47. Athauda, T. J.; Hari, P.; Ozer, RR. Tuning Physical and Optical Properties of ZnO Nanowire Arrays Grown on Cotton Fibers. *ACS Appl. Mater. Interfaces.* **2013**, *5*, 6237-6246.
48. Xia, X.; Zhang, J.; Sawall T. A simple colorimetric method for the quantification of Au(III) ions and its use in quantifying Au nanoparticles. *Anal. Methods*, **2015**, *7*, 3671-3675.

49. Zhang, S.; Zhang, Z.; Wang, T.; Zhang, D.; Li, X.; Xue, Z.; Shan, D.; Lu, X. High-throughput and ultratrace naked-eye colorimetric detection of Au³⁺ based on the gold amalgam-stimulated peroxidase mimetic activity in aqueous solutions. *Chem. Commun.*, **2017**, 53, 5056-5058.

Appendix A

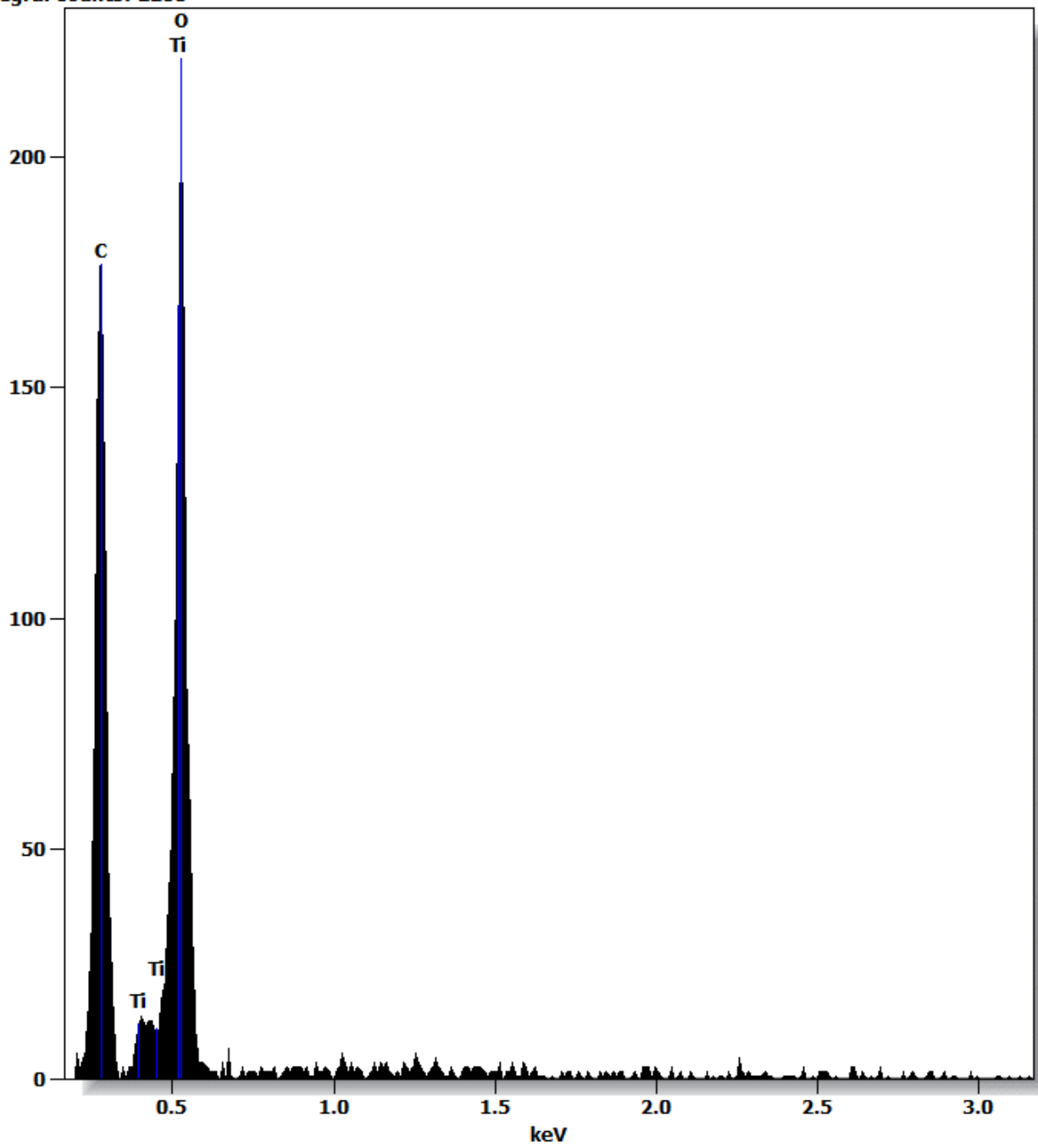
Binary system EDX Line analysis data.

1. CF@TiO₂ composite material.

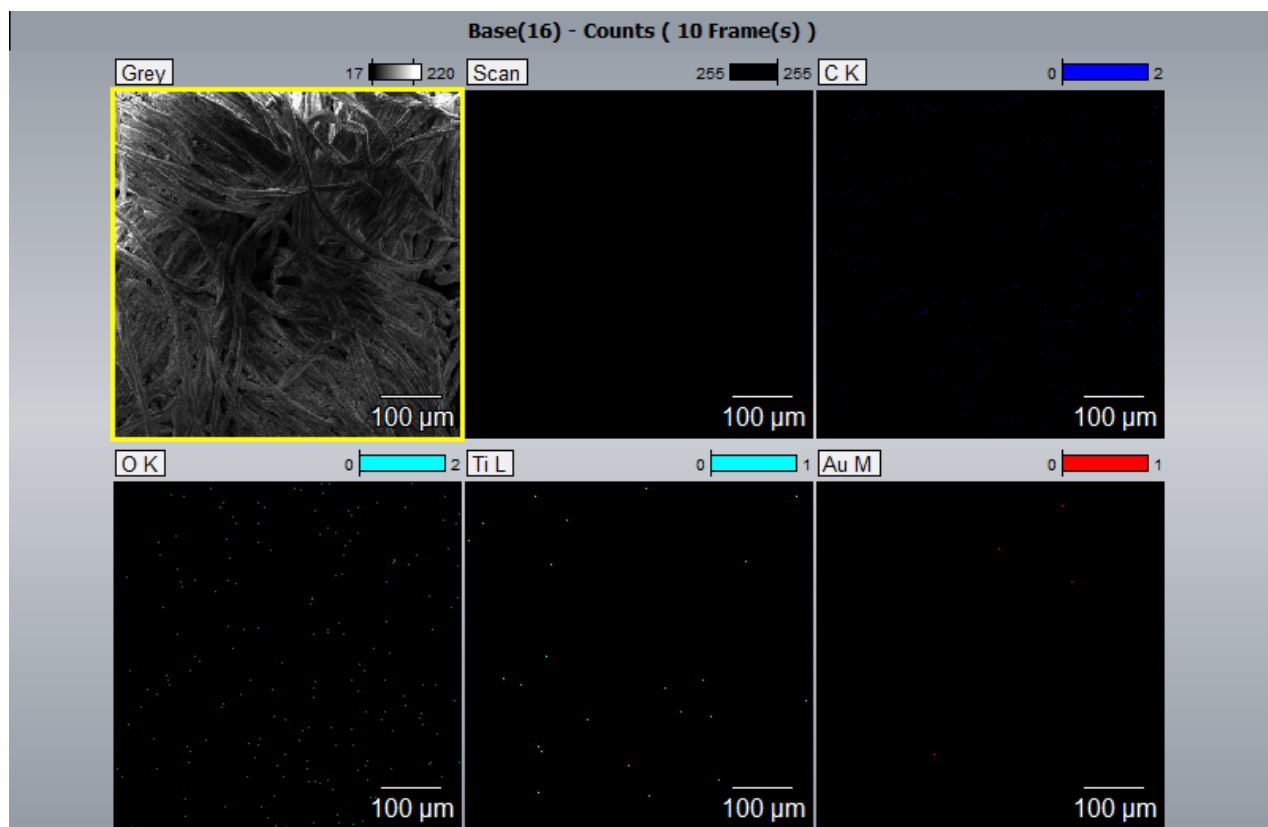


Full scale counts: 222
Integral Counts: 2280

Base(13)

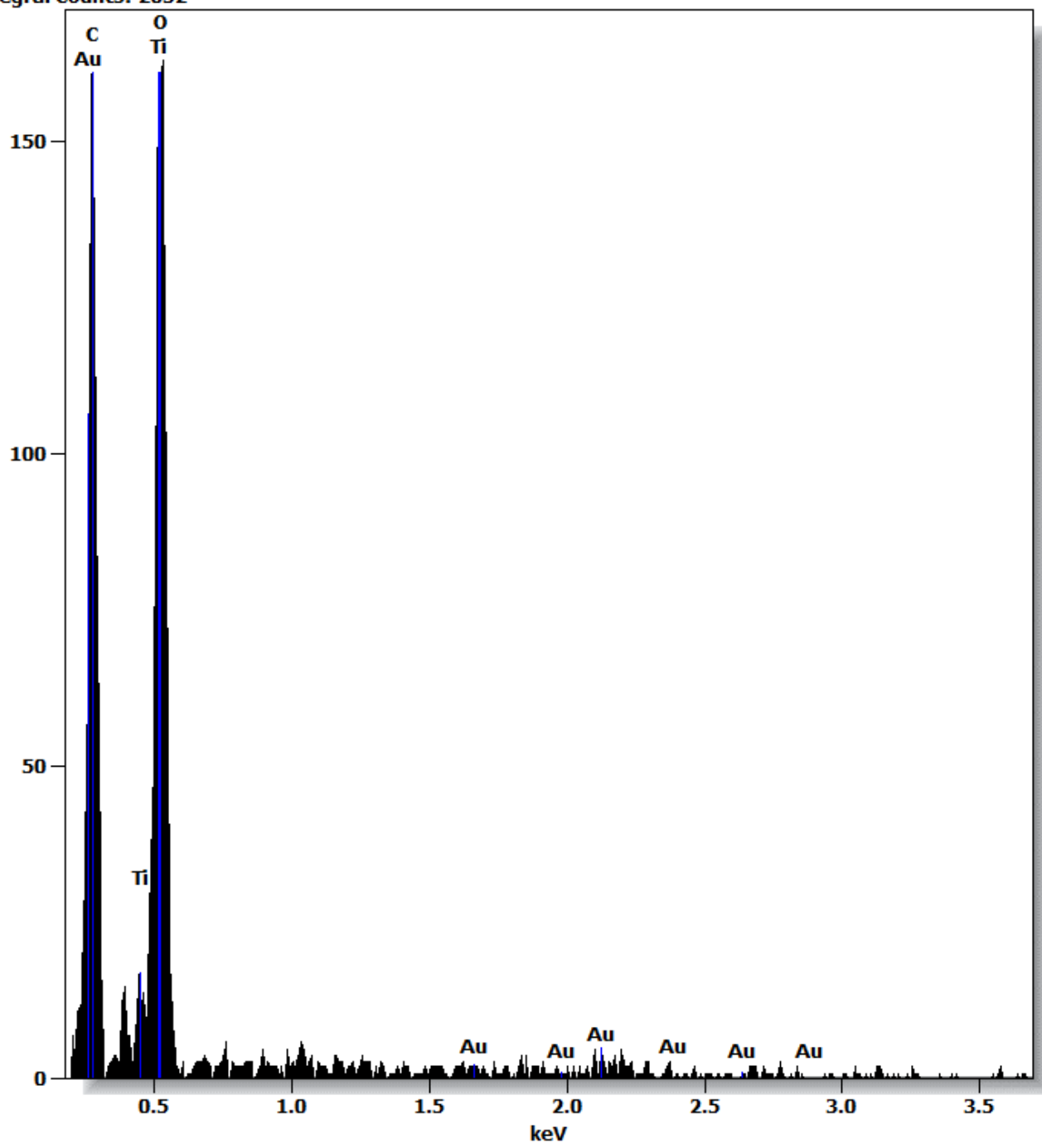


2. CF@TiO₂-AuNPs composite material.



Full scale counts: 164
Integral Counts: 2052

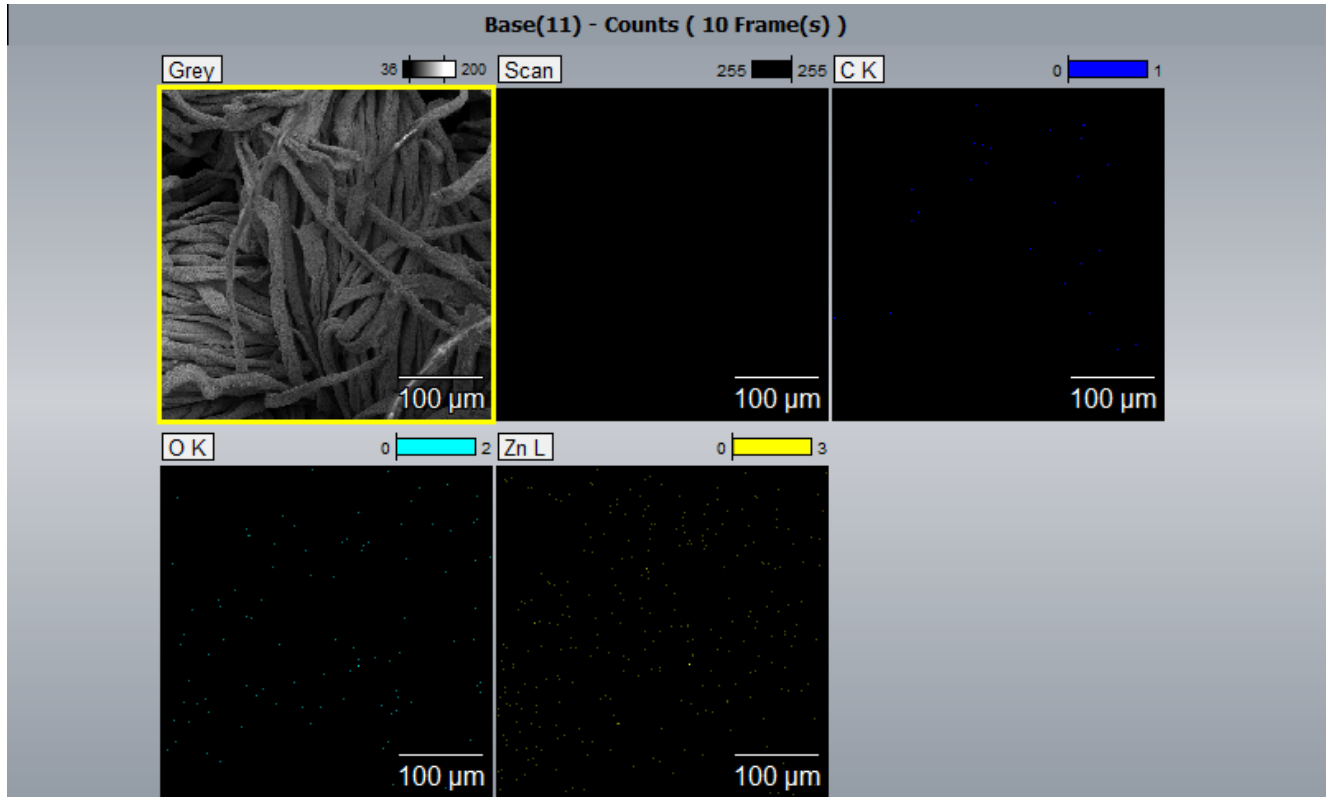
Base(16)



Appendix B

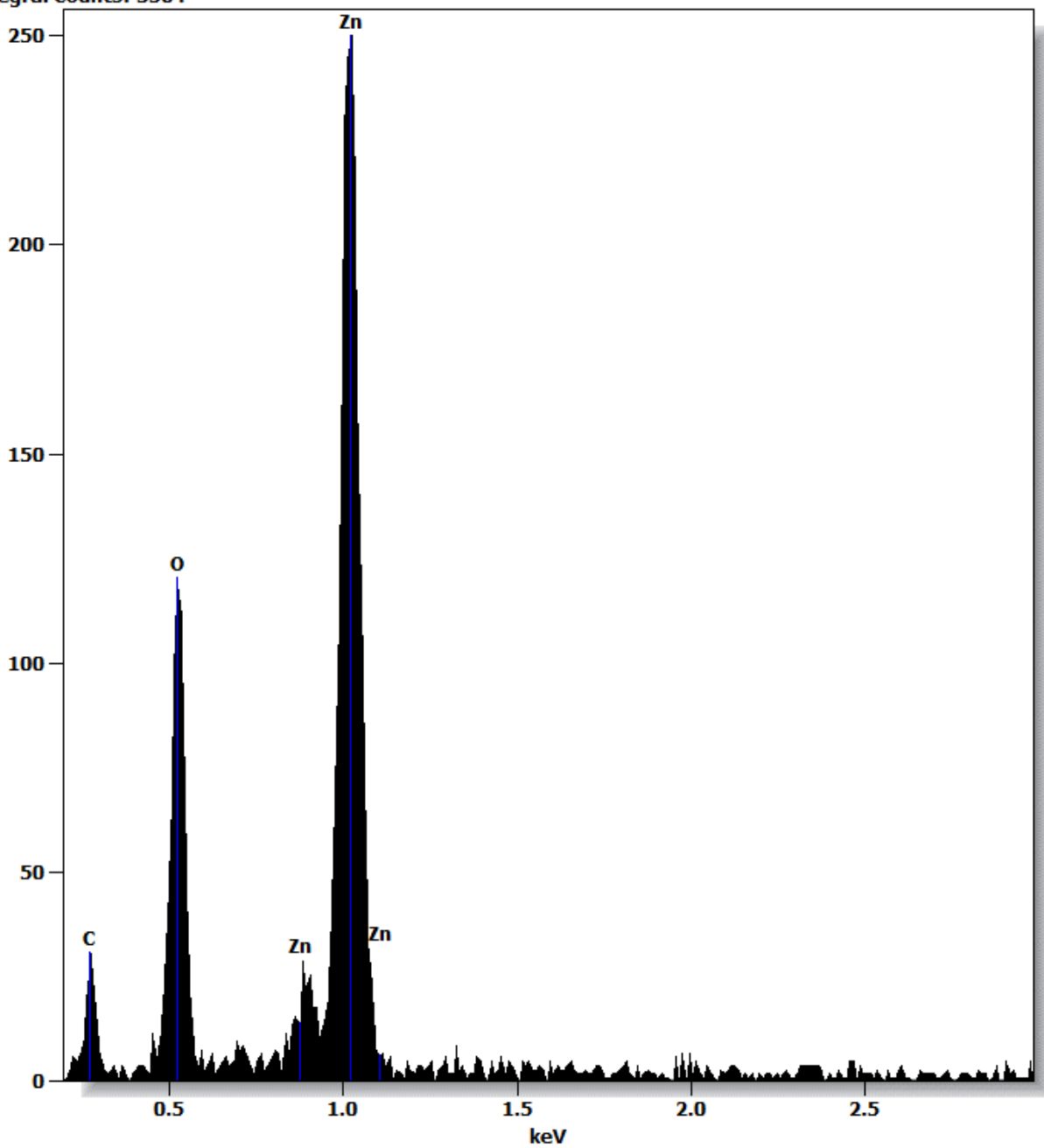
Ternary system EDX Line analysis data.

1. CF@ZnONRs composite material.

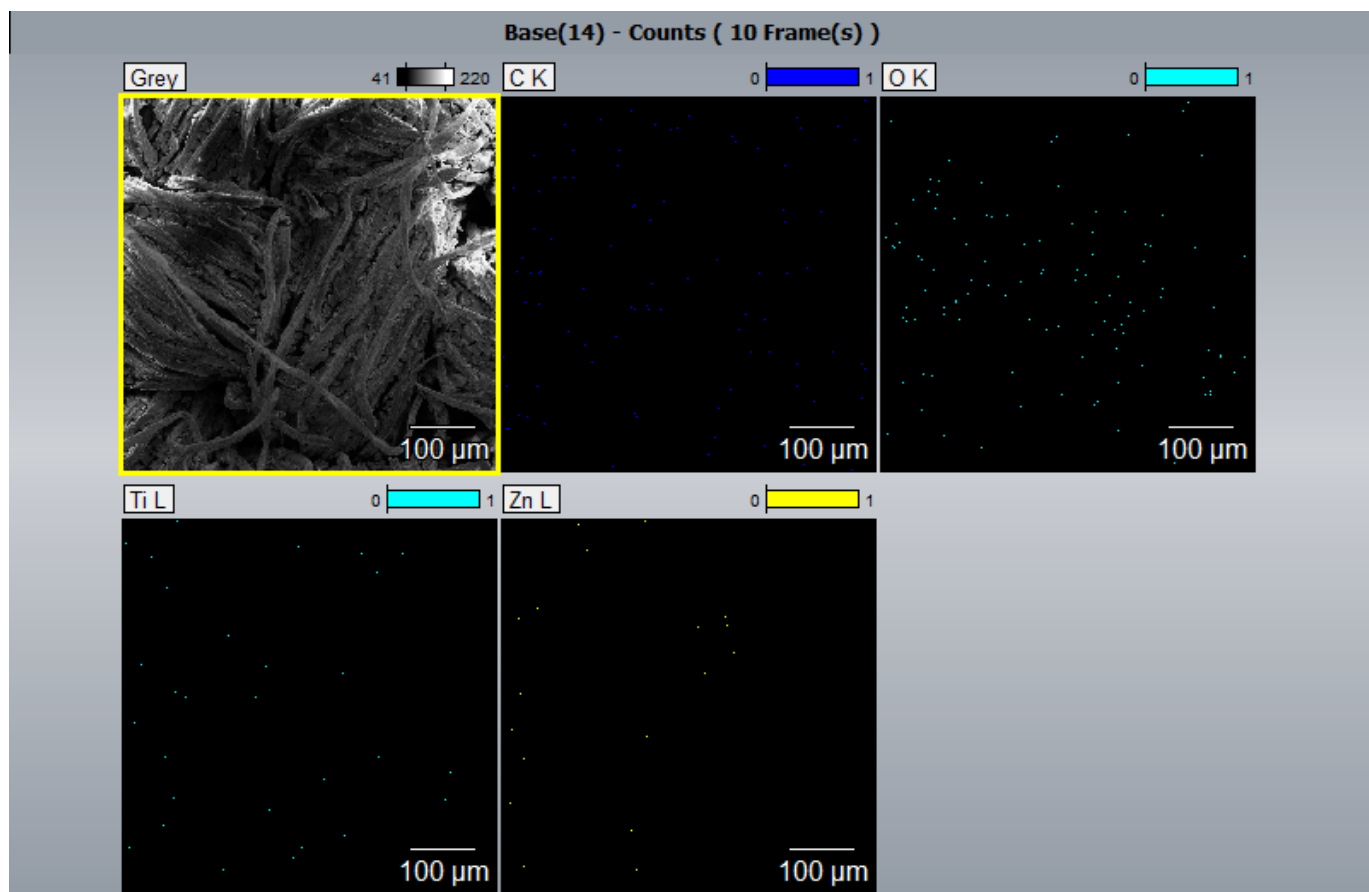


Full scale counts: 251
Integral Counts: 3504

Base(11)

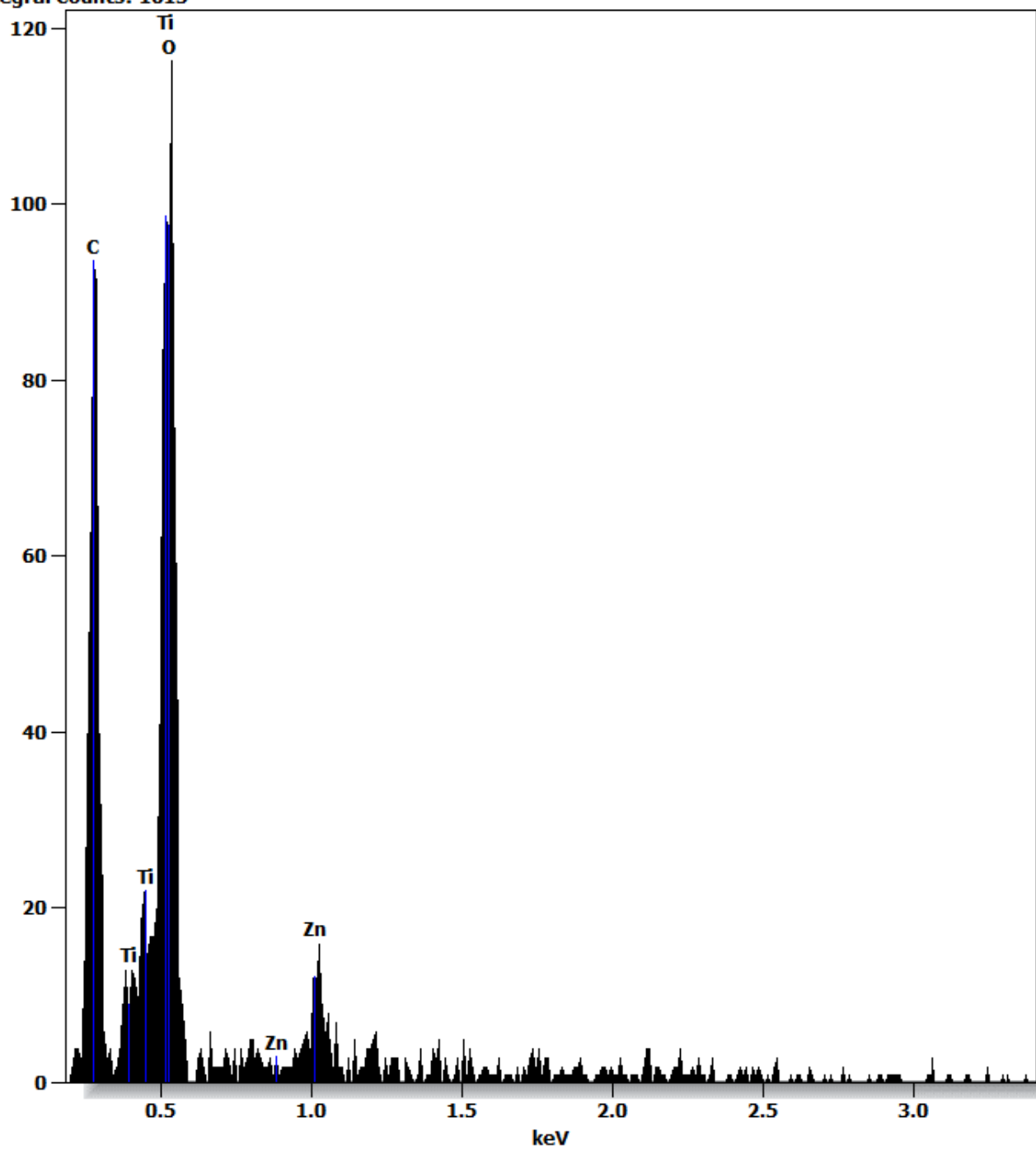


2. CF@ZnONRs-TiO₂ composite material.

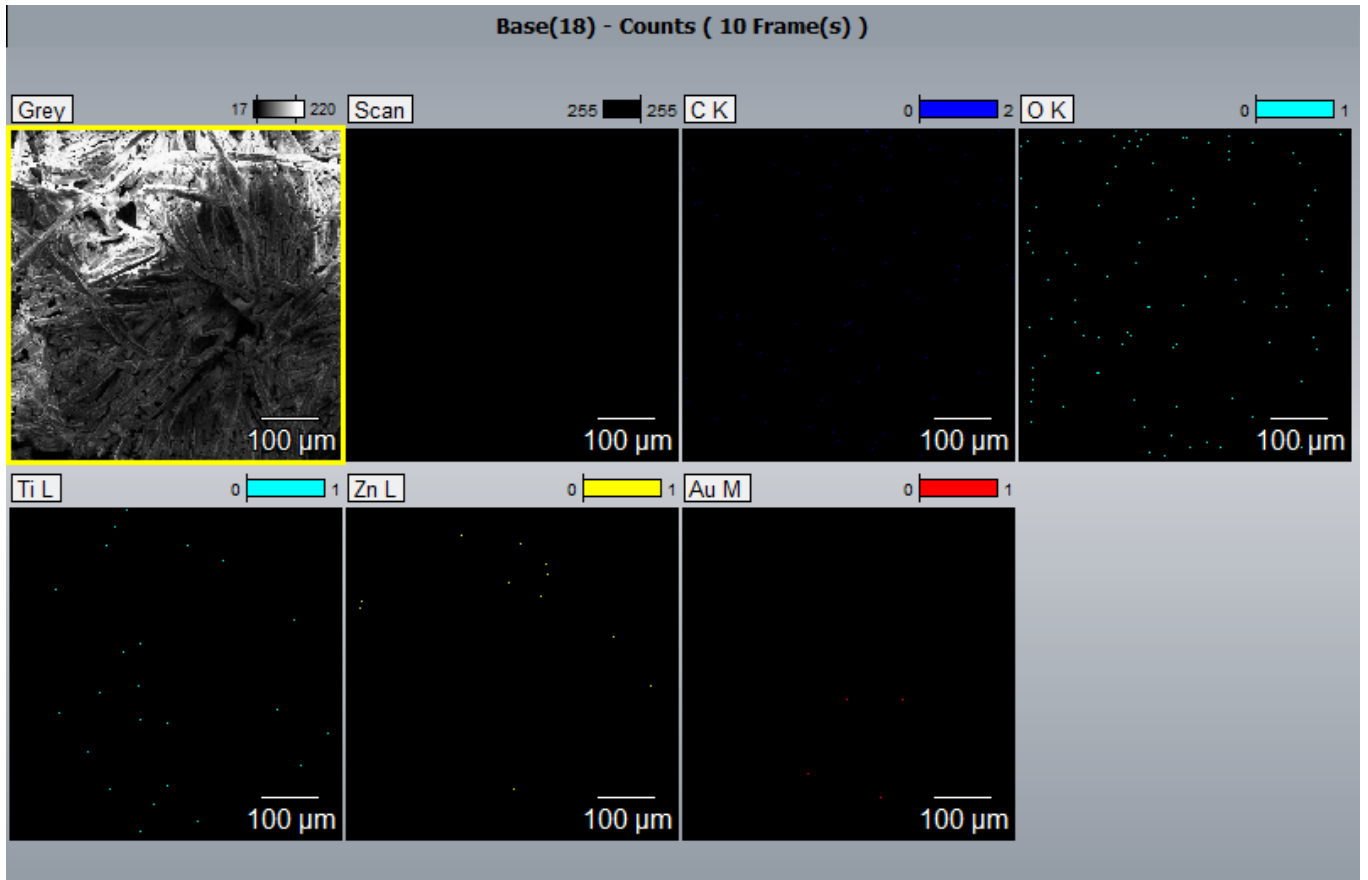


Full scale counts: 117
Integral Counts: 1615

Base(14)



3. CF@ZnONRs-TiO₂-AuNPs composite material.



Full scale counts: 122
Integral Counts: 1633

Base(18)

